

# Dust attenuation in $2 < z < 3$ star-forming galaxies from deep ALMA observations of the *Hubble Ultra Deep Field*

R. J. McLure<sup>1\*</sup>, J.S. Dunlop<sup>1</sup>, F. Cullen<sup>1</sup>, N. Bourne<sup>1</sup>, P.N. Best<sup>1</sup>, S. Khochfar<sup>1</sup>,  
R.A.A. Bowler<sup>2</sup>, A.D. Biggs<sup>3</sup>, J.E. Geach<sup>4</sup>, D. Scott<sup>5</sup>, M.J. Michałowski<sup>6,1</sup>,  
W. Rujopakarn<sup>7,8,9</sup>, E. van Kampen<sup>3</sup>, A. Kirkpatrick<sup>10</sup>, A. Pope<sup>11</sup>

<sup>1</sup>*Institute for Astronomy, University of Edinburgh, Royal Observatory, Edinburgh, EH9 3HJ, UK*

<sup>2</sup>*Astrophysics, The Denys Wilkinson Building, University of Oxford, Keble Road, Oxford, OX1 3RH, UK*

<sup>3</sup>*European Southern Observatory, Karl-Schwarzschild-Str. 2, 95748 Garching b. Munchen, Germany*

<sup>4</sup>*Centre for Astrophysics Research, Science & Technology Research Institute, University of Hertfordshire, Hatfield, AL10 9AB, UK*

<sup>5</sup>*Department of Physics and Astronomy, University of British Columbia, Vancouver, BC V6T1Z1, Canada*

<sup>6</sup>*Astronomical Observatory Institute, Faculty of Physics, Adam Mickiewicz University, ul. Słoneczna 36, 60-286 Poznań, Poland*

<sup>7</sup>*Department of Physics, Faculty of Science, Chulalongkorn University, 254 Phayathai Road, Pathumwan, Bangkok 10330, Thailand*

<sup>8</sup>*National Astronomical Research Institute of Thailand (Public Organization), Donkaew, Maerim, Chiangmai 50180, Thailand*

<sup>9</sup>*Kavli Institute for the Physics and Mathematics of the Universe (WPI), The University of Tokyo, Kashiwa, Chiba 277-8583, Japan*

<sup>10</sup>*Yale Center for Astronomy & Astrophysics, Physics Department, P.O. Box 208120, New Haven, CT 06520, USA*

<sup>11</sup>*Department of Astronomy, University of Massachusetts, Amherst, MA 01002, USA*

Accepted XXX. Received YYY; in original form ZZZ

## ABSTRACT

We present the results of a new study of the relationship between infrared excess ( $\text{IRX} \equiv L_{\text{IR}}/L_{\text{UV}}$ ), UV spectral slope ( $\beta$ ) and stellar mass at redshifts  $2 < z < 3$ , based on a deep Atacama Large Millimeter Array (ALMA) 1.3-mm continuum mosaic of the *Hubble Ultra Deep Field* (HUDF). Excluding the most heavily-obscured sources, we use a stacking analysis to show that  $z \approx 2.5$  star-forming galaxies in the mass range  $9.25 \leq \log(M_*/M_\odot) \leq 10.75$  are fully consistent with the  $\text{IRX}-\beta$  relation expected for a relatively grey attenuation curve, similar to the commonly adopted Calzetti law. Based on a large, mass complete, sample of  $2 \leq z \leq 3$  star-forming galaxies drawn from multiple surveys, we proceed to derive a new empirical relationship between  $\beta$  and stellar mass, making it possible to predict UV attenuation ( $A_{1600}$ ) and  $\text{IRX}$  as a function of stellar mass, for any assumed attenuation law. Once again, we find that  $z \approx 2.5$  star-forming galaxies follow  $A_{1600}-M_*$  and  $\text{IRX}-M_*$  relations consistent with a relatively grey attenuation law, and find no compelling evidence that star-forming galaxies at this epoch follow a reddening law as steep as the Small Magellanic Cloud (SMC) extinction curve. In fact, we use a simple simulation to demonstrate that previous determinations of the  $\text{IRX}-\beta$  relation may have been biased toward low values of  $\text{IRX}$  at red values of  $\beta$ , mimicking the signature expected for an SMC-like dust law. We show that this provides a plausible mechanism for reconciling apparently contradictory results in the literature and that, based on typical measurement uncertainties, stellar mass provides a cleaner prediction of UV attenuation than  $\beta$ . Although the situation at lower stellar masses remains uncertain, we conclude that for  $2 < z < 3$  star-forming galaxies with  $\log(M_*/M_\odot) \geq 9.75$ , both the  $\text{IRX}-\beta$  and  $\text{IRX}-M_*$  relations are well described by a Calzetti-like attenuation law.

**Key words:** galaxies: high-redshift – galaxies: evolution – galaxies: starburst – galaxies: star formation – submillimetre: galaxies

## 1 INTRODUCTION

Obtaining an accurate measurement of the evolution of the cosmic star-formation rate density remains a key goal in observational

cosmology. A thorough, pre-ALMA, review of our understanding of the evolution of the cosmic star-formation rate density (SFRD) from both the UV and far-infrared (FIR) was provided by [Madau & Dickinson \(2014\)](#). The data assembled for this review clearly demonstrate the dominant contribution made by obscured star formation over the redshift range  $0 < z < 3$ , and the remarkably good

\* E-mail: rjm@roe.ac.uk

agreement between FIR and dust-corrected UV star-formation rate densities over the same redshift interval. However, it is worth noting that the exact location of the peak in cosmic SFRD is still uncertain, as is the steepness of the decline in SFRD to higher redshift (e.g. Dunlop et al. 2017; Novak et al. 2017). Moreover, due to the limited sensitivity of FIR and radio observations, our current knowledge of the SFRD at  $z \geq 3$  is still largely confined to dust-corrected measurements of the integrated UV luminosity density derived from studies of Lyman-break galaxies (e.g. McLure et al. 2013; McLeod et al. 2016; Finkelstein 2016; Stark 2016).

Within this context, the vastly improved sensitivity at sub-mm and mm-wavelengths provided by ALMA affords an unprecedented opportunity to measure the contribution of obscured star formation at  $z \geq 3$ . For example, the individual detections and stacking results derived from the deep 1.3-mm ALMA mosaic of the HUDF presented by Dunlop et al. (2017) confirmed the dominant contribution of obscured star formation (by a factor of 2–5) around the peak in cosmic SFRD at  $z \approx 2$ . However, the results presented in Dunlop et al. (2017) also indicated that a sharp fall-off in obscured star formation at higher redshifts means that the SFRD is dominated by the unobscured UV component at  $z \geq 4$ , a result subsequently confirmed by a stacking analysis of the deepest available sub-mm imaging from the SCUBA-2 Cosmology Legacy Survey (Bourne et al. 2017).

Despite the improved sensitivity provided by ALMA, it is clear that assembling an accurate picture of the evolution of cosmic SFRD still requires a method for reliably dust correcting rest-frame UV measurements. Traditionally this dust correction is made using the so-called Meurer relation:  $A_{1600} = 1.99\beta + 4.43$ , which relates the observed UV spectral slope (i.e.  $\beta$  where  $f_\lambda \propto \lambda^\beta$ ) of star-forming galaxies to the absolute level of dust attenuation at 1600Å (Meurer et al. 1999). The Meurer relation is itself derived from the IRX– $\beta$  relation, where IRX (infrared excess) is usually defined as the ratio of infrared to UV luminosity ( $L_{\text{IR}}/L_{\text{UV}}$ ). Under the assumption that star-forming galaxies all have similar *intrinsic* UV slopes, and that their infrared luminosity arises from dust heated by the same UV continuum, it is possible to show that IRX maps uniquely to  $A_{1600}$  (Meurer et al. 1999).

The great utility of the Meurer relation is that it allows dust-corrected star-formation rates to be derived based on nothing more than an apparently straightforward measurement of UV luminosity and spectral slope and, as a consequence, its functional form and potential evolution with redshift has been the focus of sustained interest (e.g. Kong et al. 2004; Reddy et al. 2010; Overzier et al. 2011; Takeuchi et al. 2012; Lee et al. 2012; Capak et al. 2015; Salmon et al. 2016; Popping et al. 2017; Narayanan et al. 2018).

However, two sets of observational results in the recent literature have led to renewed interest in the validity and evolution of the IRX– $\beta$  relation. Firstly, spectroscopic observations have revealed that the physical conditions (including ionization parameter and metallicity) within star-forming galaxies at  $z \geq 2$  are systematically different to those of their low-redshift counterparts (e.g. Shapley et al. 2015; Steidel et al. 2016; Cullen et al. 2016; Strom et al. 2017). Secondly, several recent ALMA measurements of dust continuum emission in  $z \geq 2$  star-forming galaxies appear to suggest that at least some high-redshift galaxies produce significantly less IR luminosity than predicted by the Meurer relation (e.g. Capak et al. 2015; Bouwens et al. 2016; Koprowski et al. 2016; Pope et al. 2017; Fudamoto et al. 2017), and appear to follow an IRX– $\beta$  relation more compatible with an SMC-like *extinction* law. Indeed, the recent results presented by Reddy et al. (2018) suggest that the bluest galaxies at  $1.5 < z < 2.5$  agree with the IRX– $\beta$  relation

predicted by the SMC extinction law, provided that their intrinsic UV slopes are ultra-blue (i.e.  $\beta_{\text{int}} \approx -2.6$ ).

The apparently low IRX values displayed by some high-redshift galaxies can be viewed as surprising from two different perspectives. Firstly, theoretical studies (e.g. Witt & Gordon 2000; Seon & Draine 2016) have shown that dust properties that produce steep extinction laws (i.e. SMC-like) produce attenuation curves, appropriate for dust correcting integrated galaxy photometry, which are much greyer in the UV<sup>1</sup>. Secondly, recent studies investigating the functional form of dust reddening in high-redshift galaxies (e.g. Reddy et al. 2015; Scoville et al. 2015; Cullen et al. 2017) have tended to conclude that dust attenuation at  $\lambda_{\text{rest}} < 2500$  is similarly grey to the Calzetti et al. (2000) starburst attenuation law, which predicts an IRX– $\beta$  relation virtually indistinguishable from the Meurer relation.

Adding to the confusing picture is the fact that several studies have produced individual or stacked sub-mm/mm detections for  $z \geq 3$  galaxies that are perfectly consistent with the Meurer relation (e.g. Watson et al. 2015; Coppin et al. 2015; Dunlop et al. 2017; Laporte et al. 2017). Motivated by these apparently contradictory results, in this paper we investigate the IRX– $\beta$  and IRX– $M_*$  relations at  $2 \leq z \leq 3$  using the deep ALMA 1.3-mm imaging of the HUDF presented by Dunlop et al. (2017). The structure of the paper is as follows. In Section 2 we describe the relevant data sets, our spectral energy distribution (SED) fitting and the selection of our star-forming galaxy samples. In Section 3 we briefly review the derivation of the IRX– $\beta$  relation and justify the assumptions that we adopt throughout the rest of the analysis. In Section 4 we present our IRX– $\beta$  results at  $2 \leq z \leq 3$  and compare to the recent literature. In Section 5 we use a large, mass complete, sample of star-forming galaxies at  $2 \leq z \leq 3$  to investigate the relationship between UV spectral slope, UV dust attenuation and stellar mass. In Section 6 we proceed to study the form of the IRX– $M_*$  relation at  $2 \leq z \leq 3$  in the HUDF, comparing our results to recent literature studies. In Section 7 we investigate possible biases in previous determinations of the IRX– $\beta$  relation, and present a plausible mechanism for explaining apparent discrepancies in the form of the IRX– $\beta$  and IRX– $M_*$  relations previously presented. Finally, in Section 8 we provide a summary of our results and conclusions. Throughout the paper magnitudes are quoted in the AB system (Oke & Gunn 1983) and we assume the following cosmology:  $\Omega_M = 0.3$ ,  $\Omega_\Lambda = 0.7$  and  $H_0 = 70 \text{ km s}^{-1} \text{ Mpc}^{-1}$ .

## 2 DATA AND SED FITTING ANALYSIS

In this section we provide a brief overview of the imaging data sets employed in the current study and describe the SED fitting used to derive the key parameters required for the subsequent analysis. In particular, we provide a full description of the methods used to fit the UV spectral slopes and define our final samples of star-forming galaxies.

<sup>1</sup> Throughout the paper we refer to *extinction* as the absorption and scattering of light out of the line of sight, by dust between the object and the observer - as measured when deriving extinction laws in the MW and SMC. We refer to *attenuation* as the absorption and scattering of light out of the line of sight, appropriate for a galaxy where the stars and dust are mixed together. It is the scattering of light back into the line of sight which results in the attenuation law being greyer than the corresponding extinction law.

## 2.1 ALMA data

We use the ALMA 1.3-mm continuum image of the HUDF presented by Dunlop et al. (2017). The final mosaic was constructed from 45 separate ALMA pointings and covers an area of  $4.5 \text{ arcmin}^2$ , overlapping with the ultra-deep ( $m_{\text{AB}} \simeq 30; 5\sigma$ ), near-IR *HST* imaging of the field (Ellis et al. 2013; Illingworth et al. 2013) obtained with Wide Field Camera 3 (WFC3/IR). The 1.3-mm mosaic has a uniform depth of  $35 \mu\text{Jy beam}^{-1}(1\sigma)$  at a spatial resolution of  $0.7 \text{ arcsec}$ . Full details of the observations and data reduction are provided in Dunlop et al. (2017), along with the multi-wavelength photometry and derived physical properties for the 16 sources detected with  $S_{1.3} > 120 \mu\text{Jy}$ .

## 2.2 HUDF optical/IR data

The HUDF has been the focus of many ultra-deep imaging campaigns over the last decade, following-on from the original Advanced Camera for Surveys (ACS) imaging obtained in 2003 (Beckwith et al. 2006). Of key importance to this study are the ultra-deep near-IR observations obtained with WFC3/IR during the UDF09 (Bouwens et al. 2011) and UDF12 (Ellis et al. 2013; Koekemoer et al. 2013) imaging campaigns.

The optical/near-IR imaging supplied by *HST* is supplemented by ultra-deep ground-based UV and  $K$ -band imaging obtained with the VIMOS (Nonino et al. 2009) and HAWK-I (Fontana et al. 2014) cameras on the VLT. Finally, the ultra-deep *Spitzer* IRAC imaging of the field obtained via a series of different observing campaigns (see Labbé et al. 2015 for a summary) plays a crucial role in constraining the stellar masses of high-redshift galaxies.

In this study we make use of the GOODS-S photometry catalogue provided by the CANDELS survey team (Guo et al. 2013). This catalogue provides PSF-homogenised photometry of the ACS and WFC3/IR imaging within the HUDF, in addition to resolution-matched photometry of the lower spatial resolution ground-based and *Spitzer* IRAC imaging derived using the TFIT deconvolution code (Laidler et al. 2007).

## 2.3 CANDELS optical/IR data

In order to expand the dynamic range of our star-forming galaxy sample we supplement the HUDF data with the photometry for the wider GOODS-S field provided by Guo et al. (2013). In addition, we also include the photometry assembled for the CANDELS UDS field by Galametz et al. (2013). The Galametz et al. (2013) catalogue provides equivalent PSF-homogenised UV-to-midIR photometry in the CANDELS UDS field to that provided by Guo et al. (2013) for the CANDELS GOODS-S field. We refer the reader to Galametz et al. (2013) for a full description of the ground-based and space-based imaging incorporated within the catalogue.

## 2.4 Ultra-VISTA optical/IR data

Although constituting some of the best multi-wavelength data available, the combined area of the CANDELS GOODS-S and UDS fields is  $< 0.1 \text{ deg}^2$ . Consequently, to significantly improve the statistics of our star-forming galaxy sample at high stellar-masses ( $10 \leq \log(M_*/M_\odot) \leq 11.5$ ), we also incorporate the photometry catalogue for the Ultra-VISTA (UVISTA) survey DR3 produced for the  $K$ -band luminosity function study of Mortlock et al. (2017). This catalogue includes  $u^*g'r'i'z'$  photometry from the T0007 data release of the CFHT Legacy Survey (Hudelot et al. 2012), deep

$z$ -band photometry from Subaru Suprime-Cam (Furusawa et al. 2016),  $YJHK$  imaging from UVISTA DR3 and *Spitzer* IRAC imaging from the *Spitzer* Extended Deep Survey (SEDS; Ashby et al. 2013) and *Spitzer* Large Area Survey (SPLASH; Steinhardt et al. 2014). The UVISTA photometry catalogue is split into components from the UVISTA deep and wide strips. The deep strip component has a  $5\sigma$  depth of  $K = 24.8$  in a  $2\text{-arcsec}$  diameter aperture. The wide component has a  $5\sigma$  depth of  $K = 23.9$ . Full details regarding the construction of the photometry catalogue can be found in Mortlock et al. (2017).

## 2.5 Photometric redshifts

For the HUDF, GOODS-S and UDS data sets we adopt the publicly available photometric redshifts derived by the CANDELS team based on the Guo et al. (2013) and Galametz et al. (2013) photometry catalogues (Santini et al. 2015). These photometric redshifts are derived by combining the results of many different photometric redshift analyses, using a variety of different codes; see Dahlen et al. (2013) for full details. For the UVISTA data set we adopt the photometric redshifts previously derived by Mortlock et al. (2017). These photometric redshifts are the median of five different photometric redshifts runs, using three different template-fitting codes. As discussed in detail by Mortlock et al. (2017), the photometric redshifts for all four data sets are of equally high quality, with a typical value of  $\sigma_{dz} = 0.02$  and a catastrophic outlier rate of 1–2 per cent (i.e.  $|dz| > 0.15$ ).

## 2.6 SED fitting analysis

All of the UV-to-midIR photometry assembled from the HUDF, CANDELS and UVISTA data sets was analysed with the SED fitting code originally developed by McLure et al. (2011) and then subsequently updated as described by McLeod et al. (2015). This code fits stellar-population templates to the available photometry in wavelength–flux density space to allow for the accurate handling of photometric errors and non-detections. Provided with a set of synthetic stellar-population models, the code derives the best-fitting values of photometric redshift, stellar mass, star-formation rate and dust reddening. In addition, based on the best-fitting SED template the code also calculates rest-frame photometry in a wide variety of different filters.

Throughout the main analysis pursued in this paper, the code used SED templates derived from Bruzual & Charlot (2003) stellar population models, based on a Chabrier (2003) IMF, with dust reddening described by the Calzetti et al. (2000) starburst attenuation law (with  $A_V$  in the range  $0 \leq A_V \leq 4.0$ ) and IGM absorption accounted for using the Madau (1995) prescription. The fitting considered standard  $\tau$ -model star-formation histories with values in the range  $0.3 \text{ Gyr} \leq \tau \leq 10.0 \text{ Gyr}$ , and metallicities of either solar ( $Z_\odot$ ) or one-fifth solar ( $0.2Z_\odot$ ). During the SED fitting process, templates were considered with ages between 50 Myr and the age of the Universe at the appropriate redshift.

The two physical parameters that are derived from the SED fitting and used throughout the subsequent analysis are the stellar mass and intrinsic UV spectral slope ( $\beta_{\text{int}}$ ). In order to check that our estimates are not biased by our choice of SED template set, we experimented with a wide range of star-formation histories, including exponentially decaying, constant and exponential increasing. These experiments demonstrated that the derived stellar masses are stable at the  $\pm 0.1$  dex level and the values of  $\beta_{\text{int}}$  are stable at the  $\pm 0.1$  level (using either Calzetti or SMC dust reddening).

As discussed in Section 7, the code was also used to explore the impact of low stellar-metallicity, nebular emission and stellar binaries by re-fitting the HUDF star-forming galaxy sample using the ‘Binary Population and Spectral Synthesis’ (BPASSv2) stellar population models (Eldridge & Stanway 2016; Stanway et al. 2016). Once again, the derived values of stellar mass and  $\beta_{\text{int}}$  were found to be stable to SED template choice.

## 2.7 Measuring the UV spectral slope

Several different techniques have been advocated in the literature for measuring the UV spectral slope of star-forming galaxies based on photometry alone; see Rogers et al. (2013) for a review. The techniques commonly employed range from straightforward single-colour measurements (e.g. Dunlop et al. 2013; Bouwens et al. 2012), to applying the same UV windows used to measure  $\beta$  from UV spectra (Calzetti et al. 1994) to the SED templates that provide the best-fit to the available photometry (Finkelstein et al. 2012).

Here we adopt the technique employed by Rogers et al. (2014) for their study of the colour-magnitude relation ( $\beta - M_{\text{UV}}$ ) at  $z \approx 5$ . The best-fitting value of  $\beta$  for each galaxy is determined by fitting the photometry covering the wavelength range  $1268\text{\AA} \leq \lambda_{\text{rest}} \leq 2580\text{\AA}$  with a series of pure power-law SED models, in which IGM absorption is accounted for using the Madau (1995) prescription. The photometry for each galaxy was fit with a set of power-law models covering the range  $-4.0 \leq \beta \leq +4.0$  in steps of  $\Delta\beta = 0.01$ , and the asymmetric  $\beta$  uncertainties were calculated from the  $\Delta\chi^2 = 1$  interval around the best-fitting value.

## 2.8 UVJ selection

An essential requirement for the analysis presented in this paper is a clean sample of  $2 \leq z \leq 3$  star-forming galaxies free, as far as possible, from potentially quiescent galaxies. To achieve this, we have adopted so-called *UVJ* selection, which separates quiescent and star-forming galaxies based on their positions on the rest-frame  $U - V$  vs  $V - J$  colour-colour diagram. This method was first formalised by Williams et al. (2009) and was shown to be applicable out to redshifts of at least  $z \approx 2.5$  by Whitaker et al. (2011). In addition to its ability to efficiently separate star-forming and quiescent galaxies, an important advantage of *UVJ* selection is that it is virtually independent of the choice of stellar-population templates used when deriving the rest-frame *UVJ* photometry. This is notably not the case when separating star-forming and quiescent galaxies based on a specific star-formation rate (sSFR) criterion.

Both Williams et al. (2009) and Whitaker et al. (2011) agree on the best diagonal separation between the star-forming and quiescent populations, but adopt slightly different additional criteria to prevent contamination of the passive galaxies by both unobscured and dusty star-forming galaxies. In order to minimize the contamination of our star-forming galaxy sample by potentially quiescent galaxies, we have adopted a hybrid of the Williams et al. (2009) and Whitaker et al. (2011) criteria. Specifically, any galaxy which meets all of the following criteria is classified as *potentially* quiescent and therefore excluded from the final samples:

$$\begin{aligned} U - V &> 0.88(V - J) + 0.59; \\ U - V &> 1.2; \\ V - J &< 1.6. \end{aligned} \quad (1)$$

It should be noted that a straightforward adoption of either the Williams et al. (2009) or Whitaker et al. (2011) criteria does not

significantly change the conclusions drawn from the star-forming galaxy samples in the subsequent analysis.

## 2.9 Star-forming galaxy samples at $2 < z < 3$

Throughout the rest of the analysis we will employ two samples of *UVJ*-selected star-forming galaxies within the redshift interval  $2 \leq z \leq 3$ . The first sample consists of galaxies selected from the area of the HUDF covered by the ALMA 1.3-mm mosaic. This HUDF sample is mass complete down to a limit of  $\log(M_*/M_\odot) \geq 8.50$  and is used in Sections 4–6 for the analysis of the IRX– $\beta$  and IRX– $M_*$  relations.

For the analysis of the relationship between UV spectral slope and stellar mass, we enhance the dynamic range of the HUDF sample by including *UVJ*-selected galaxies from the UDS, GOODS-S and UVISTA data sets discussed above. To ensure mass-completeness, the GOODS-S and UDS samples are restricted to  $\log(M_*/M_\odot) \geq 8.95$  and  $9.20$ , respectively. For the UVISTA data set we impose mass-completeness limits of  $\log(M_*/M_\odot) \geq 10.00$  and  $10.35$  for the UVISTA-deep and UVISTA-wide components, respectively.

Following the application of the *UVJ* selection criteria, a small number of galaxies ( $< 1\%$ ) were identified that satisfied the *UVJ* criteria as star-forming galaxies, but that have sSFRs which strongly suggest that they are in fact quiescent (i.e.  $\text{sSFR} \leq 0.1 \text{ Gyr}^{-1}$ ). The vast majority of these apparent interlopers are located in an area of parameter space ( $U - V > 2.0$ ;  $V - J > 1.6$ ) where the *UVJ* selection technique is prone to confusion between dusty star-forming galaxies and genuinely passive systems. After their removal the full, mass-complete, sample consists of 8273 star-forming galaxies at  $2 \leq z \leq 3$ , spanning an area of  $\approx 1 \text{ deg}^2$  and the stellar-mass range:  $8.50 \leq \log(M_*/M_\odot) \leq 11.50$ .

Finally, it is worth noting that the median sSFR for the full sample of  $2 \leq z \leq 3$  star-forming galaxies is  $3.0 \pm 0.1 \text{ Gyr}^{-1}$ . This can be compared to the median value of  $3.2 \text{ Gyr}^{-1}$  predicted by the Speagle et al. (2014) meta-study of star-formation ‘main sequence’ results. This comparison provides an additional level of confidence that the adopted *UVJ* selection technique has successfully isolated a sample of galaxies consistent with populating the main sequence at  $2 \leq z \leq 3$ .

## 3 THE INFRARED EXCESS

In their original study of a sample of local starburst galaxies, Meurer et al. (1999) defined the infrared excess IRX as:

$$\text{IRX} \equiv \frac{F_{\text{FIR}}}{F_{1600}}, \quad (2)$$

where  $F_{1600}$  is the observed flux at  $\lambda_{\text{rest}} = 1600$ , defined as  $F_{1600} = \nu S_\nu$ , and the far infrared flux is defined as:

$$F_{\text{FIR}} = 1.25 [F(60) + F(100)], \quad (3)$$

where  $F(60)$  and  $F(100)$  are the fluxes measured by *IRAS* in the 60  $\mu\text{m}$  and 100  $\mu\text{m}$  bands (Helou et al. 1988). Under the assumption that the infrared luminosity of a galaxy represents reprocessed emission from dust heated by the UV photons produced by an actively star-forming stellar population, Meurer et al. (1999) showed that IRX can be accurately approximated as:

$$\text{IRX} = B \left( 10^{0.4A_{1600}} - 1 \right), \quad (4)$$

where  $A_{1600}$  is the attenuation at  $\lambda_{\text{rest}} = 1600$  in magnitudes, and the multiplicative factor was calculated by Meurer et al. (1999) to



have a value of  $B = 1.19 \pm 0.20$ . The multiplicative factor is actually the ratio of two bolometric correction factors:

$$B = \frac{\text{BC}(1600)}{\text{BC}(\text{FIR})}, \quad (5)$$

where the numerator effectively converts between  $F_{1600}$  and total flux available to heat the dust, and the denominator converts between  $F_{\text{FIR}}$  and the bolometric IR flux emitted by the dust.

Throughout the analysis presented in this paper, as is common practice for studies of high-redshift galaxies, we adopt the following IRX definition:

$$\text{IRX} \equiv \frac{L_{\text{IR}}}{L_{\text{UV}}}, \quad (6)$$

where  $L_{\text{IR}}$  is the total IR luminosity (8–1000  $\mu\text{m}$ ) and  $L_{\text{UV}}$  is  $\lambda L_{\lambda}$  evaluated at 1600  $\text{\AA}$ . Using this definition,  $\text{BC}(\text{FIR}) = 1$  and the multiplicative factor is simply  $B = \text{BC}(1600)$ . Here we take an empirical approach to setting the value of  $\text{BC}(1600)$ , adopting the median value of  $\text{BC}(1600) = 1.71 \pm 0.05$  derived from the SED fits to the full  $2 < z < 3$  sample of star-forming galaxies defined in Section 2. Consequently, throughout this study we adopt the following relationship between IRX and  $A_{1600}$ :

$$\text{IRX} = 1.71 \left( 10^{0.4A_{1600}} - 1 \right), \quad (7)$$

noting that this normalization is consistent with that adopted by many previous studies, which typically fall within the range  $1.66 < \text{BC}(1600) < 2.08$  (e.g. Meurer et al. 1999; Reddy et al. 2010; Overzier et al. 2011; Cullen et al. 2017).

In practice, when deriving IRX values for both individual objects and stacked data, we calculate the ratio of  $\text{SFR}_{\text{IR}}$  to  $\text{SFR}_{\text{UV}}$ . To calculate  $\text{SFR}_{\text{IR}}$  we adopt the results of the template fitting performed on the full long-wavelength (24  $\mu\text{m}$ –1.3 mm) SEDs of the detected ALMA objects presented in Dunlop et al. (2017). For the objects within the redshift interval  $2 < z < 3$ , the results of this SED fitting indicate that

$$\text{SFR}_{\text{IR}} / \text{M}_{\odot} \text{yr}^{-1} \approx 0.3 \times (S_{1.3} / \mu\text{Jy}), \quad (8)$$

where  $S_{1.3}$  is the 1.3-mm ALMA flux density. This calibration is virtually identical to first calculating  $L_{\text{IR}}$  from the 1.3-mm flux, assuming an optically thin modified blackbody spectrum with a dust temperature of  $T_{\text{dust}} = 35$  K and a dust emissivity index of  $\beta_{\text{dust}} = 1.6$ , and then applying:

$$\log \left( \text{SFR}_{\text{IR}} / \text{M}_{\odot} \text{yr}^{-1} \right) = \log (L_{\text{IR}} / W) - 36.44, \quad (9)$$

which is the  $\text{SFR}_{\text{IR}}$  calibration from Kennicutt & Evans (2012), converted to a Chabrier (2003) IMF.

To calculate the value of  $\text{SFR}_{\text{UV}}$  we adopt the following calibration:

$$\log \left( \text{SFR}_{\text{UV}} / \text{M}_{\odot} \text{yr}^{-1} \right) = \log (L_{\text{UV}} / W) - 36.44, \quad (10)$$

where  $L_{\text{UV}}$  is calculated from the absolute magnitude at 1500  $\text{\AA}$  derived from the best-fitting SED templates to the available UV-to-midIR photometry. This calibration is taken from Madau & Dickinson (2014), and has again been converted to a Chabrier (2003) IMF. It can be seen from equations (9) and (10) that with our choice of SFR calibrations

$$\text{IRX} \equiv \frac{L_{\text{IR}}}{L_{\text{UV}}} \equiv \frac{\text{SFR}_{\text{IR}}}{\text{SFR}_{\text{UV}}}. \quad (11)$$

As a result, we will use IRX and the ratio of IR to UV star-formation rate interchangeably throughout the rest of the paper.

### 3.1 Connecting IRX and dust reddening

In principle, equation (7) allows the value of IRX to be estimated based solely on a measurement of  $A_{1600}$ . However, given that a direct measurement of  $A_{1600}$  is impractical, in practice it is necessary to make the further assumption that before dust attenuation, the intrinsic UV spectral slopes (i.e.  $\beta_{\text{int}}$ ) of all actively star-forming galaxies are very similar. If this assumption is valid then, for a given assumed form of the underlying attenuation law, it is possible to calculate  $A_{1600}$  based on a measurement of the *observed* UV spectral slope (i.e.  $\beta_{\text{obs}}$ ), since:

$$A_{1600} = \frac{dA_{1600}}{d\beta} (\beta_{\text{obs}} - \beta_{\text{int}}), \quad (12)$$

where the slope of the reddening law has the values

$$\frac{dA_{1600}}{d\beta} = 1.99, \quad \frac{dA_{1600}}{d\beta} = 1.97, \quad \frac{dA_{1600}}{d\beta} = 0.91, \quad (13)$$

for the Meurer et al. (1999) relation, the Calzetti et al. (2000) starburst attenuation law and the SMC extinction law, respectively. The slope of the SMC extinction law adopted here is based on the derivation of Gordon et al. (2003), although earlier studies of UV extinction in the SMC by (e.g. Prevot et al. 1984) produce a virtually identical value for the slope. We note that our calculations of the dust law slopes assume that  $\beta$  is measured between  $\lambda_1 = 1276 \text{\AA}$  and  $\lambda_2 = 2490 \text{\AA}$ , the centres of the first and last UV windows defined by Calzetti et al. (1994). Other values quoted in the literature are the result of different choices of wavelength anchors. For example, changing to  $\lambda_1 = 1600 \text{\AA}$  results in dust law slopes of  $dA_{1600}/d\beta \approx 2.2$  and  $dA_{1600}/d\beta \approx 1.2$  for the Calzetti et al. (2000) attenuation and SMC extinction laws respectively.

It can be seen from equation (13) that the slope of the reddening law implied by the Meurer et al. (1999) relation and the Calzetti et al. (2000) attenuation law are virtually identical. As a consequence, throughout this paper we will consistently plot IRX curves corresponding to the Calzetti et al. (2000) attenuation law, noting that the IRX curves corresponding to the Meurer et al. (1999) relation are virtually indistinguishable.

As highlighted in the introduction, dust properties that produce a steep *extinction* law (e.g. SMC or MW), will inevitably produce an *attenuation* law that is much shallower<sup>2</sup> (i.e. greyer). Therefore, when dealing with integrated galaxy photometry, it is unlikely that the effective attenuation curve will be as steep as the SMC extinction law. However, despite this, throughout the paper we will also consistently plot predicted IRX curves based on the SMC extinction law, for two reasons. Firstly, as noted by Pettini et al. (1998), the SMC curve does serve as a useful lower-limit to the amount of UV attenuation. Secondly, as noted in the introduction, there have been several claims in the recent literature that the IRX– $\beta$  relation followed by high-redshift galaxies is closer to the predictions of the SMC extinction law, than the original Meurer/Calzetti relation.

For completeness, our final adopted IRX relations are as follows:

$$\text{IRX} = 1.71 \left( 10^{0.4 \times 1.97 (\beta_{\text{obs}} - \beta_{\text{int}})} - 1 \right) \quad [\text{Calzetti}] \quad (14)$$

$$\text{IRX} = 1.71 \left( 10^{0.4 \times 0.91 (\beta_{\text{obs}} - \beta_{\text{int}})} - 1 \right) \quad [\text{SMC}] \quad (15)$$

where  $\beta_{\text{obs}}$  is the observed value of the UV spectral slope and  $\beta_{\text{int}}$  is the assumed intrinsic value. Throughout this analysis, we adopt

<sup>2</sup> Where steep and shallow refer to large or small values of  $\frac{d\beta}{dA_{1600}}$ .

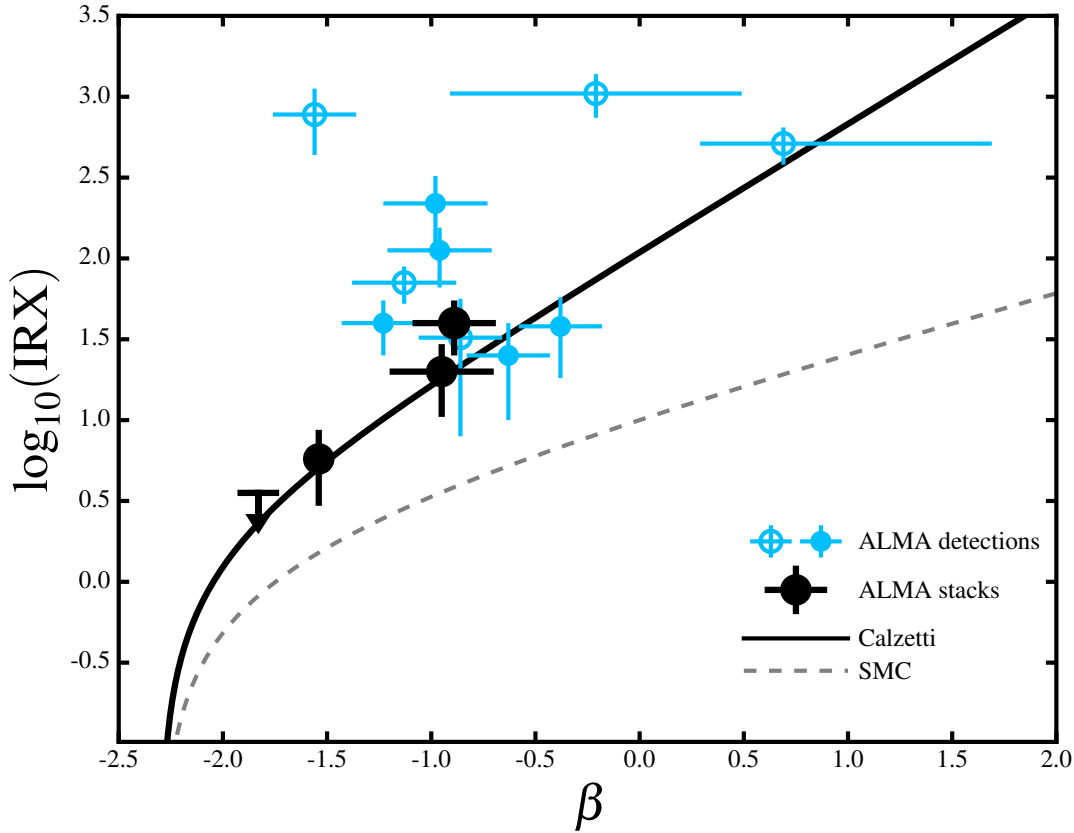


**Figure 1.** The IRX– $\beta$  relation for  $2 \leq z \leq 3$  star-forming galaxies within the HUDF. The black upper limit ( $2\sigma$ ) corresponds to a stack of  $2 \leq z \leq 3$  galaxies from our HUDF star-forming galaxy sample with stellar masses in the range  $8.50 \leq \log(M_*/M_\odot) < 9.25$ . The black data-point at  $\beta = -1.54 \pm 0.05$  corresponds to a stack of  $2 \leq z \leq 3$  HUDF star-forming galaxies in the mass range  $9.25 \leq \log(M_*/M_\odot) < 10.00$ . The two black data points at  $\beta \approx -0.9$  both correspond to stacks within the mass range  $10.00 \leq \log(M_*/M_\odot) < 10.75$ . The higher of the two data points is a stack of all galaxies within the stellar mass bin, including sources that were individually detected at  $S_{1.3} > 120 \mu\text{Jy}$ . The lower of the two data points is a stack of those objects that were not individually detected. The solid black line is the predicted IRX– $\beta$  relation under the assumption that the underlying dust curve follows the Calzetti et al. (2000) attenuation law. The dashed grey line is the predicted IRX– $\beta$  relation under the assumption that the underlying dust curve follows the SMC extinction law (e.g. Gordon et al. 2003). The blue data points are ten galaxies with redshifts in the range  $1.72 < z < 3.08$ , which were identified in the 1.3-mm ALMA mosaic of the HUDF with  $S_{1.3} > 120 \mu\text{Jy}$  by Dunlop et al. (2017). The solid blue data points show the ALMA-detected objects which are included in the black stacked data points (i.e. those objects with  $2 \leq z \leq 3$  and  $8.50 \leq \log(M_*/M_\odot) < 10.75$ ). The open blue data points show the ALMA-detected objects which are not included in the stacked data points due to having a redshift outside the range  $2 \leq z \leq 3$ , or  $\log(M_*/M_\odot) > 10.75$ .

$\beta_{\text{int}} = -2.3$ , which is the median value of the intrinsic UV spectral slope based on the SED fitting of our sample of  $2 < z < 3$  star-forming galaxies in the HUDF. We note that this is similar to the canonical value of  $\beta_{\text{int}} = -2.23$  adopted by Meurer et al. (1999).

#### 4 IRX VERSUS UV SLOPE

In Fig. 1 we show the IRX– $\beta$  relation for star-forming galaxies at  $z \approx 2.5$ , based on our analysis of the deep ALMA 1.3-mm mosaic of the HUDF. The blue data points show the ten galaxies within the redshift range  $1.72 < z < 3.08$  that were detected in the ALMA mosaic with  $S_{1.3} \geq 120 \mu\text{Jy}$ . The IRX values for these objects are based on the  $\text{SFR}_{\text{IR}}$  and  $\text{SFR}_{\text{UV}}$  estimates derived by Dunlop et al. (2017), and are plotted with  $\beta$  values based on our power-law SED fitting. The solid black data points show the ALMA-detected objects which are included in the black data points derived via stacking into the ALMA mosaic (see Section 4.1). The open blue data points show

the ALMA-detected objects which are not included in the stacked data points due to having a redshift outside the range  $2 \leq z \leq 3$ , or  $\log(M_*/M_\odot) > 10.75$ . The solid black and dashed grey lines show the expected IRX– $\beta$  relations for Calzetti and SMC-like dust laws (equations 14 and 15) under the assumption that  $\beta_{\text{int}} = -2.3$ .

As can be seen from Fig. 1, those objects that were individually detected in the HUDF 1.3-mm mosaic are either consistent with the Calzetti IRX– $\beta$  relation, or lie significantly above it. It is of course entirely expected that heavily-obscured objects will lie above the IRX– $\beta$  relation, simply because the fundamental dust-screen assumption underlying the derivation of equation (7) will not hold for the most heavily obscured sources. Indeed, many of the individually detected objects in the ALMA 1.3-mm mosaic show spatial off-sets between the obscured and unobscured star-formation (Rujopakarn et al. 2016).

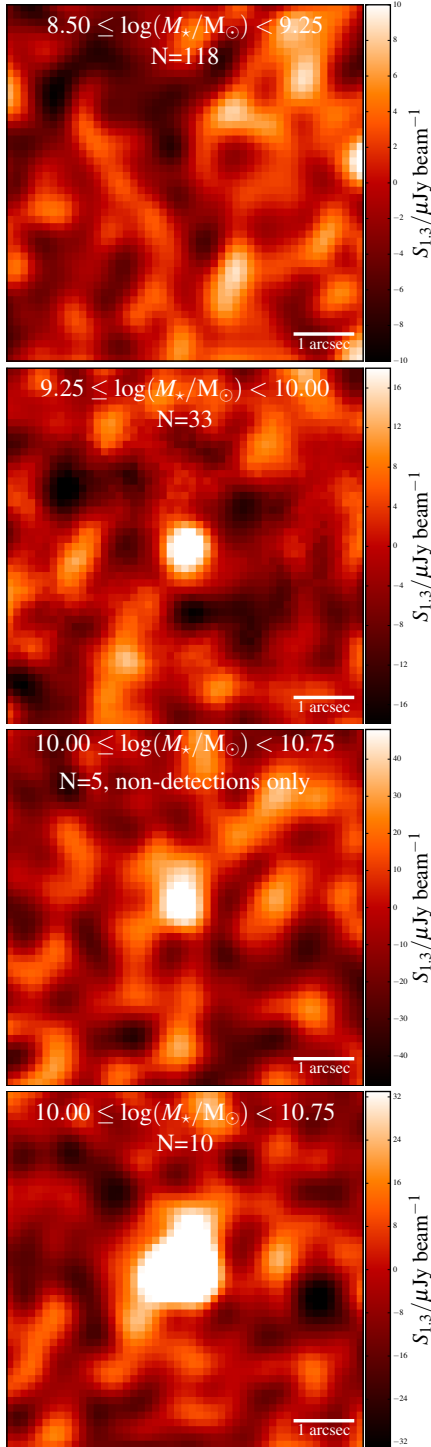


**Figure 2.** Mean ALMA 1.3-mm stacks of  $2.0 < z < 3.0$  star-forming galaxies in the HUDF. The top stack is a non-detection ( $2\sigma$  upper limit  $\approx 6 \mu\text{Jy}$ ) for galaxies in the stellar-mass range  $8.50 \leq \log(M_*/M_\odot) < 9.25$ . The second stack is a  $6\sigma$  detection for galaxies in the stellar-mass range  $9.25 \leq \log(M_*/M_\odot) < 10.00$ . The third stack is a  $4\sigma$  detection for galaxies in the mass range  $10.00 \leq \log(M_*/M_\odot) < 10.75$ , which are not *individually* detected at  $S_{1.3} > 120 \mu\text{Jy}$  ( $3.5\sigma$  significance). The final stack consists of all galaxies within this last mass range, including 5/16 of the  $S_{1.3} > 120 \mu\text{Jy}$  sources identified by Dunlop et al. (2017).

#### 4.1 Stacking results

The black data points in Fig. 1 show the results of stacking the ALMA data for those  $2.0 \leq z \leq 3.0$  star-forming galaxies in the HUDF with stellar masses in the following ranges (left-to-right):  $8.50 \leq \log(M_*/M_\odot) < 9.25$ ,  $9.25 \leq \log(M_*/M_\odot) < 10.00$  and  $10.00 \leq \log(M_*/M_\odot) < 10.75$ . For each stellar-mass bin, we first calculate the individual values of IRX for each object entering the bin (including negative values of IRX corresponding to negative ALMA fluxes), and then plot the unweighted mean value of IRX at the corresponding unweighted mean value of  $\beta$ .

The final mass bin has been split into two data points, the higher of which shows the result of stacking all ten galaxies within the  $10.00 \leq \log(M_*/M_\odot) < 10.75$  mass bin. Five of these ten galaxies (solid blue data points in Fig. 1) were individually detected at  $S_{1.3} \geq 120 \mu\text{Jy}$  ( $\geq 3.5\sigma$ ) by Dunlop et al. (2017). The lower data point in the figure corresponds to a stack of the five galaxies within this mass bin that were not individually detected at  $\geq 3.5\sigma$  by Dunlop et al. (2017). The data point for the  $8.50 \leq \log(M_*/M_\odot) < 9.25$  stellar-mass bin is a robust  $2\sigma$  upper limit (i.e. measured value  $+2\sigma$ ). The stacked images corresponding to the four black data points are shown in Fig. 2.

As can be seen from Fig. 1, the first three stellar-mass bins are all perfectly consistent with the IRX– $\beta$  relation expected for Calzetti-like dust attenuation, although the upper limit is obviously also consistent with an SMC-like dust curve. The stacked data point which includes five objects detected with  $S_{1.3} \geq 120 \mu\text{Jy}$  (solid blue data points in Fig. 1), lies a factor of  $\approx 2$  above the Calzetti IRX– $\beta$  relation. This is entirely consistent with the results presented in Dunlop et al. (2017), which indicated that SED template fitting using the Calzetti et al. (2000) attenuation law was capable of recovering the total (i.e. UV+IR) star-formation rate for galaxies with  $\log(M_*/M_\odot) \leq 10.3$ , but under-estimated the total star-formation rate by approximately a factor of two at higher masses.

The results presented in Fig. 1 for both individual objects and stellar-mass stacks strongly suggest that the IRX– $\beta$  relation for star-forming galaxies at  $z \approx 2.5$  is fully consistent with that expected for Calzetti-like dust attenuation. In contrast, there is no indication from these results that the effective dust attenuation at this epoch is as steep as the SMC extinction curve (at least for  $\beta_{\text{int}} \approx -2.3$ ). This surprisingly clear result is in apparent contrast to the wide variety of different results that have been presented in the recent literature.

#### 4.2 Comparison to recent literature results

In Fig. 3 we show a compilation of results from a number of different studies of the IRX– $\beta$  relation taken from the recent literature (Heinis et al. 2013; Álvarez-Márquez et al. 2016; Bouwens et al. 2016; Bourne et al. 2017; Fudamoto et al. 2017; Reddy et al. 2018). Crucially, all of these studies focused on samples of star-forming galaxies within the redshift interval  $1.5 \leq z \leq 3$ , and featured infrared luminosities derived from *Herschel*, SCUBA-2 or ALMA data.

In common with this study, the results of both Bouwens et al. (2016) and Fudamoto et al. (2017) are based on mm-wavelength imaging with ALMA. In their study, Bouwens et al. (2016) investigated the IRX– $\beta$  relation of  $1.5 < z < 3$  Lyman break galaxies (LBGs), based on an independent 1.2-mm ALMA mosaic within the HUDF. This mosaic is slightly deeper than the 1.3-mm mosaic studied here, but covers an area which is approximately four times smaller. The recent study of Fudamoto et al. (2017) is based on

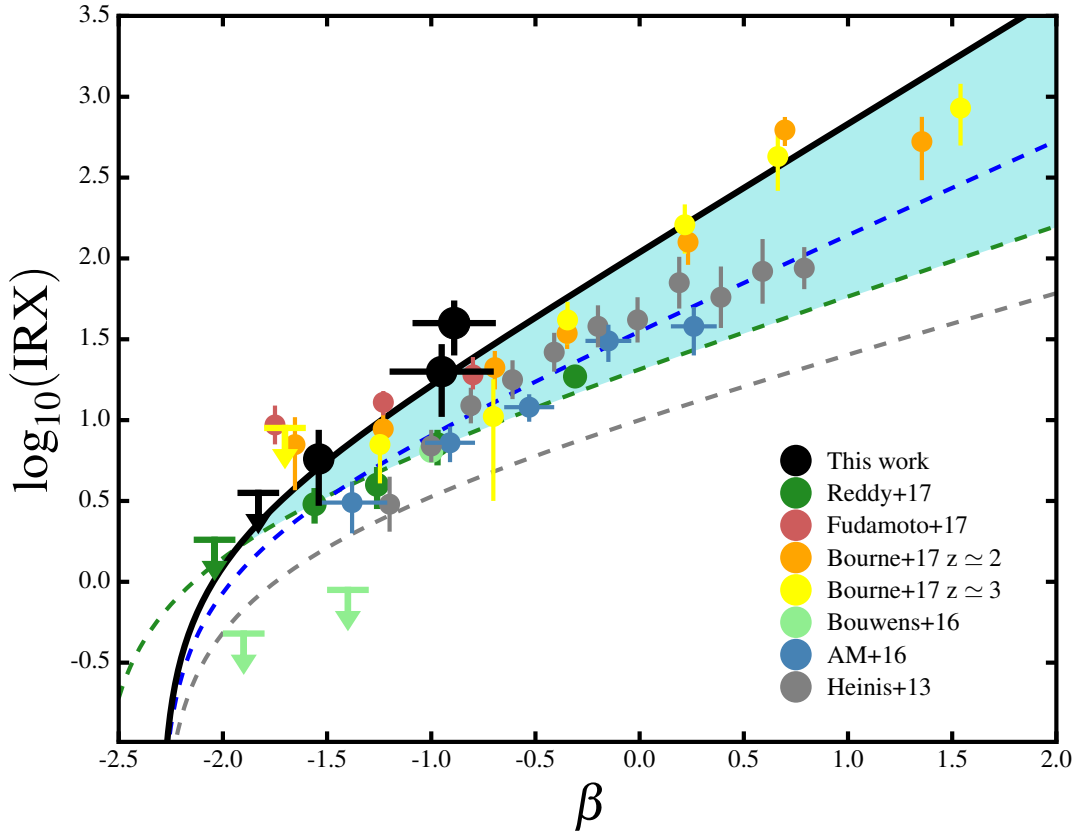


**Figure 3.** A compilation of IRX– $\beta$  results from the recent literature for star-forming galaxies within the redshift interval  $1.5 \leq z \leq 3$ . In addition to the new results derived in this work (black data points), we have plotted the results from the following studies: [Heinis et al. \(2013\)](#), [Álvarez-Márquez et al. \(2016\)](#), [Bouwens et al. \(2016\)](#), [Bourne et al. \(2017\)](#), [Fudamoto et al. \(2017\)](#) and [Reddy et al. \(2018\)](#). As in Fig. 1, the solid black and dashed grey lines show the expected IRX– $\beta$  relations for Calzetti-like and SMC-like dust curves. The dark green dashed line shows the IRX– $\beta$  relation derived by [Reddy et al. \(2018\)](#). The blue dashed line shows the IRX– $\beta$  relation for a dust curve with a slope in the UV that is intermediate to the Calzetti and SMC-like relations (see text for details). The blue shading highlights the region into which observational measurements of the IRX– $\beta$  relation are likely to scatter, even when the underlying IRX– $\beta$  relation is close to the Calzetti-like prediction (black line); see Section 7 for a full discussion.

ALMA Band 6 continuum observations of 67 massive star-forming galaxies in the COSMOS field with a median redshift of 3.2.

[Álvarez-Márquez et al. \(2016\)](#) studied the IRX– $\beta$  relation using a sample of LBGs at  $2.5 < z < 3.5$  within the COSMOS field, using stacked *Herschel* PACS (100 and 160  $\mu\text{m}$ ), SPIRE (250, 350 and 500  $\mu\text{m}$ ) and AzTEC 1.1-mm imaging to derive infrared luminosities. Similarly, [Heinis et al. \(2013\)](#) used stacked SPIRE data (250, 350 and 500  $\mu\text{m}$ ) to study the IRX– $\beta$  relation for a sample of UV-selected galaxies at  $z \approx 1.5$  within the COSMOS field.

In their recent study, [Reddy et al. \(2018\)](#) investigated the IRX– $\beta$  relation for *UVJ*-selected star-forming galaxies at  $1.5 < z < 2.5$ , exploiting UV imaging from the Hubble Deep UV Legacy survey within the two GOODS fields. To derive their infrared luminosities, [Reddy et al. \(2018\)](#) stacked into the available short-wavelength *Herschel* PACS data (100 and 160  $\mu\text{m}$ ).

Finally, the recent study of [Bourne et al. \(2017\)](#) stacked the deepest available 450– and 850– $\mu\text{m}$  imaging from the SCUBA-2 Cosmology Legacy Survey (CLS; [Geach et al. 2017](#)), in combination with 100, 160 and 250– $\mu\text{m}$  *Herschel* imaging, to determine the infrared luminosities of *UVJ*-selected star-forming galaxies within three of the CANDELS survey fields. Using UV data from catalogues constructed by the 3D-HST survey team ([Brammer et al.](#)

[2012](#); [Momcheva et al. 2016](#)), [Bourne et al. \(2017\)](#) studied the form of the IRX– $\beta$  relation for star-forming galaxies over the redshift interval  $0.5 < z < 6.0$ . In Fig. 3 we plot the IRX– $\beta$  results for their galaxy sub-samples at  $z \approx 2$  and  $z \approx 3$ .

Taken at face value, the compilation of literature results shown in Fig. 3 indicates that the IRX– $\beta$  relation displayed by  $1.5 < z < 3.0$  star-forming galaxies lies roughly equidistant from the expected relations for Calzetti-like and SMC-like dust laws. Consequently, there are a limited number of options available to account for differences in the observed data, provided that one is happy to accept the basic tenet that the IRX– $\beta$  relation results from the dust attenuation of star-forming galaxies, all of which have very similar *intrinsic* UV slopes.

The first option is to assume that the intrinsic UV slope of star-forming galaxies at this epoch is  $\beta_{\text{int}} \approx -2.3$ , as indicated by the SED fitting performed here. In this case, the most straightforward interpretation of the data is that the effective attenuation law at this epoch has a slope intermediate to that of the [Calzetti et al. \(2000\)](#) and SMC dust laws (i.e.  $dA_{1600}/d\beta \approx 1.45$ ). As an illustration, the blue dashed curve in Fig. 3 shows the IRX– $\beta$  relation corresponding to equation (7), combined with  $A_{1600} = 1.45\beta - 3.34$ . This IRX– $\beta$  relation corresponds to a dust law with slope  $dA_{1600}/d\beta \approx 1.45$  and



$\beta_{\text{int}} = -2.3$ . It can be seen that this provides a reasonable fit to the data from the literature over a wide range of observed UV slope, and is similar to the IRX– $\beta$  relations derived by Heinis et al. (2013) and Álvarez-Márquez et al. (2016).

The second option is to adopt an SMC-like dust law and assume that the intrinsic UV-slopes of galaxies at this epoch are extremely blue. This is the conclusion reached by Reddy et al. (2018), based on their recent study of star-forming galaxies at  $1.5 < z < 3.0$ . The green dashed line in Fig. 3 shows the preferred solution of Reddy et al. (2018), which is based on SMC-like reddening ( $\delta A_{1600}/\delta\beta = 1.07$ ) and an assumed value of  $\beta_{\text{int}} = -2.62$ . Reddy et al. (2018) argue that the relationship between IRX and  $\beta$  effectively de-couples at UV slopes redder than  $\beta_{\text{obs}} \simeq -0.5$ , although it can be seen that their IRX– $\beta$  relation systematically underestimates the observed IRX values from most other studies at  $\beta > -1.0$ .

One of the motivations given by Reddy et al. (2018) for their adoption of  $\beta_{\text{int}} = -2.62$ , was that a BPASSv2 stellar population model with this intrinsic value of UV slope is a good match to the stacked UV spectra of 30 star-forming galaxies at  $z \simeq 2.4$  presented by Steidel et al. (2016). In Section 7 we investigate the impact of SED fitting with the BPASSv2 stellar-population models, including the contribution from nebular emission, and find that the typical values of  $\beta_{\text{int}}$  are significantly redder.

There is also a third option that is worth considering. It is possible that the true IRX– $\beta$  relation of galaxies at this epoch does lie close to the Calzetti-like prediction, with  $\beta_{\text{int}} \simeq -2.3$ . In this scenario, the observed IRX– $\beta$  data from the literature is explained by a systematic bias towards lower IRX values at red values of  $\beta$ . As explored in more detail in Section 7, a bias must be introduced at some level by the process of binning-up galaxy samples by  $\beta_{\text{obs}}$  and, for plausible levels of uncertainty in individual  $\beta_{\text{obs}}$  measurements, might be expected to scatter data into the shaded region highlighted in Fig. 3. In this scenario, our new ALMA-based IRX– $\beta$  results are less biased than some previous determinations in the literature, simply because they are based on binning in stellar mass rather than  $\beta$ , a conclusion supported by the simulation work presented in Section 7.

Fortunately, it is possible to gain crucial information on which of these three possibilities provides the best explanation of the observed IRX– $\beta$  data, by studying the relationship between stellar mass and UV attenuation in more detail.

## 5 THE RELATIONSHIP BETWEEN STELLAR MASS AND UV ATTENUATION

Given that the UV attenuation ( $A_{1600}$ ) is not directly observable, in order to study the  $A_{1600} - M_*$  relation it is necessary to employ an observational proxy. The standard method for achieving this is to use IRX as the observational proxy for  $A_{1600}$  (i.e. via equation 7). However, under the assumption that all star-forming galaxies have the same, or at least very similar, *intrinsic* UV slopes, it is also possible to use the observed UV slope ( $\beta_{\text{obs}}$ ) as an observational proxy for  $A_{1600}$ .

In the recent literature there have been numerous studies that have investigated the relationship between  $\beta$  and absolute UV magnitude, the so-called colour-magnitude relation (CMR), for Lyman break galaxies at  $4 \leq z \leq 8$  (e.g. Rogers et al. 2014; Dunlop et al. 2013; Finkelstein et al. 2012; Bouwens et al. 2014). The motivation behind these studies is to use the evolution of the CMR to gain insight into the relationship between UV luminosity, stellar population age/metallicity and dust reddening. Although useful

for constraining dust attenuation at high redshift (e.g. Cullen et al. 2017), the concentration on UV luminosity is largely through necessity, with accurate stellar masses difficult to measure at high redshift. In this section we investigate the relationship between stellar mass and UV spectral slope for star-forming galaxies at  $2 \leq z \leq 3$ , taking advantage of the availability of deep *Spitzer* IRAC data, sampling rest-frame wavelengths of  $\lambda_{\text{rest}} \simeq 1\mu\text{m}$ , to deliver the necessary robust stellar-mass estimates.

### 5.1 UV slope versus stellar mass

The left-hand panel of Fig. 4 shows  $\beta_{\text{obs}}$  versus stellar mass for the full sample of UVJ–selected star-forming galaxies at  $2 \leq z \leq 3$ . The underlying 2D histogram shows the distribution of the galaxies on the  $\beta_{\text{obs}} - M_*$  plane, while the black data points show the median values of  $\beta_{\text{obs}}$  in twelve  $\Delta M_* = 0.25$  dex mass bins, spanning the full dynamic range of the sample. The red curve shows the best-fitting third-order polynomial to the error-weighted data, and has the following form:

$$\beta_{\text{obs}} = -1.136 + 0.589X + 0.130X^2 + 0.106X^3, \quad (16)$$

where  $X = \log(M_*/10^{10} M_\odot)$ . A fit to the binned data points produces a virtually identical result. The right-hand panel of Fig. 4 shows intrinsic UV-slope ( $\beta_{\text{int}}$ ) versus stellar mass, where  $\beta_{\text{int}}$  has been measured from the best-fitting SED templates, before the application of dust reddening. It can be seen that the distribution of intrinsic UV slopes is fully consistent with a constant value of  $\beta_{\text{int}} = -2.3 \pm 0.15$  over the full range in stellar mass, where the quoted uncertainty is the standard deviation rather than the standard error.

It should be noted that the relatively small scatter around  $\beta_{\text{int}} = -2.3$  is not an inevitable consequence of our choice of SED templates. Indeed, the templates used to measure the intrinsic UV slopes, which included reddening based on both the Calzetti et al. (2000) and SMC dust curves, cover the range  $-2.75 \leq \beta_{\text{int}} \leq -1.55$ . Moreover, we recovered a virtually identical result for the median value of  $\beta_{\text{int}}$  when we re-fitted the star-forming galaxies in the HUDF with low-metallicity BPASSv2 stellar population models, including the contribution from binary stars and nebular line and continuum emission (see Section 7.2).

Fundamentally, the  $\beta_{\text{int}}$  results shown in the right-hand panel of Fig. 4 provide reassurance that the increase in  $\beta_{\text{obs}}$  shown in the left-hand panel can be attributed to increasing dust attenuation, rather than increasing stellar population age/metallicity.

### 5.2 The $A_{1600} - M_*$ relation

The immediate utility of equation (16) is that, for a given assumption about the form of the attenuation law in the UV (equation 12) and the value of  $\beta_{\text{int}}$ , it provides a direct prediction of the form of the  $A_{1600} - M_*$  relation. For example, for the Calzetti et al. (2000) attenuation law and  $\beta_{\text{int}} = -2.3$ :

$$A_{1600} = 2.293 + 1.160X + 0.256X^2 + 0.209X^3, \quad (17)$$

where  $X = \log(M_*/10^{10} M_\odot)$ . This relation is shown as the solid black line in Fig. 5, along with the equivalent relations for the Gordon et al. (2003) SMC extinction law (solid grey line) and a dust law with an intermediate UV slope to the Calzetti and SMC dust laws (solid blue line), all with  $\beta_{\text{int}} = -2.3$ . In addition, the black data points show the results of our stacking analysis, where we have converted between IRX and  $A_{1600}$  using equation (7). In Fig. 5 we

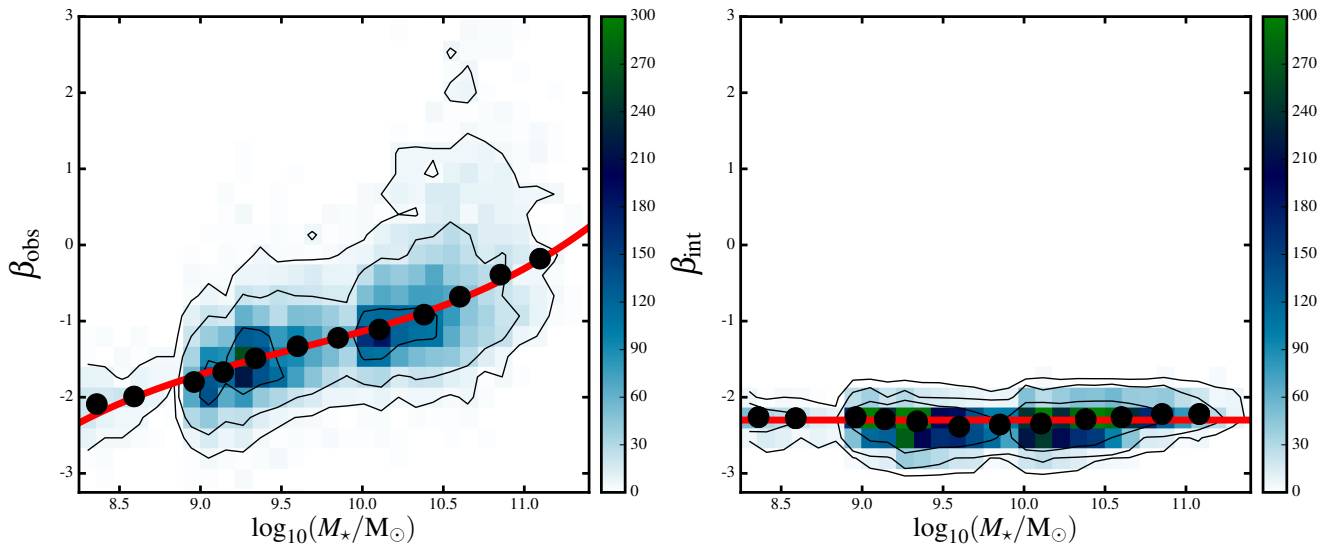


**Figure 4.** The left-hand panel shows observed UV spectral slope ( $\beta_{\text{obs}}$ ) versus stellar mass for our mass-complete sample of  $2.0 < z < 3.0$  star-forming galaxies selected from the HUDF, CANDELS GOODS-S, CANDELS UDS and UVISTA surveys (see text for details). The background image shows a 2D histogram of the  $\beta_{\text{obs}}-M_*$  distribution. The black data-points show the median values of  $\beta_{\text{obs}}$  in stellar-mass bins of width 0.25 dex (uncertainties are smaller than the data points). The red line shows the best-fitting polynomial (equation 16) to the individual, error-weighted, galaxies (a fit to the binned data points produces a virtually identical result). The right-hand panel shows intrinsic UV slope ( $\beta_{\text{int}}$ ) versus stellar mass for the same sample. The background image shows a 2D histogram of the  $\beta_{\text{int}}-M_*$  distribution, while the black data points again show the median values binned by stellar mass. The values of  $\beta_{\text{int}}$  have been measured from the best-fitting SED templates, prior to the addition of dust attenuation. The red line shows a constant value of  $\beta_{\text{int}} = -2.3$ , which is consistent with the data over the full stellar-mass range.

also plot  $A_{1600}-M_*$  relations derived from the results of six different literature studies. Five of these studies are focused on the properties of star-forming galaxies in the redshift range  $1.5 < z < 3.0$ . The final study defines the local  $A_{1600}-M_*$  relation, and is based on a large sample of star-forming galaxies drawn from the SDSS (Garn & Best 2010).

Álvarez-Márquez et al. (2016) provided binned measurements of  $A_{\text{FUV}}$  as a function of stellar mass for a large statistical sample of  $2.5 < z < 3.5$  LBGs in the COSMOS field. The definition of  $A_{\text{FUV}}$  used by Álvarez-Márquez et al. (2016) is virtually identical to our definition of  $A_{1600}$  (i.e. equation 7) and consequently, the blue dashed curve in Fig. 5 shows our linear fit to their binned  $A_{\text{FUV}}$  data. Heinis et al. (2014) provide a relation between IRX and stellar mass at  $z \approx 1.5$ , based on their study of UV-selected galaxies in COSMOS. To produce the red curve shown in Fig. 5 we have converted their IRX- $M_*$  relation into a  $A_{1600}-M_*$  relation using equation (7).

Pannella et al. (2015) investigated the dust attenuation properties of a large sample of UVJ-selected star-forming galaxies at  $z \leq 4$  in the GOODS-N field, based on stacking the ultra-deep *Herschel* PACS and SPIRE data. To plot the purple dashed curve shown in Fig. 5, we have used their  $A_{\text{UV}}-M_*$  relation at  $z \approx 2.3$  and corrected for the difference between their definition of  $A_{\text{UV}}$  and our definition of  $A_{1600}$ . We have also decreased the Pannella et al. (2015) stellar-mass estimates by 0.22 dex in order to convert from a Salpeter (1955) to a Chabrier (2003) IMF.

### 5.2.1 Conversion from nebular to continuum attenuation

The other three  $A_{1600}-M_*$  relations plotted in Fig. 5 are derived from studies which originally provided a measurement of the nebular attenuation experienced by the  $\text{H}\alpha$  emission line ( $A_{\text{H}\alpha}$ ). Garn & Best (2010) and Kashino et al. (2013) measured  $A_{\text{H}\alpha}$  via the Balmer

decrement for galaxies at  $z \approx 0$  and  $z \approx 1.5$ , respectively, while Ibar et al. (2013) obtained a measurement of  $A_{\text{H}\alpha}$  at  $z \approx 1.5$  by matching observed  $\text{H}\alpha$  and integrated IR luminosities.

To plot these relations in Fig. 5 it is necessary to both convert between attenuation at  $\lambda_{\text{rest}} = 6563$  and  $\lambda_{\text{rest}} = 1600$ , and to estimate the ratio of nebular-to-continuum attenuation in  $z \approx 2.5$  star-forming galaxies. When deriving their stellar attenuation curve from local starburst galaxies, Calzetti et al. (1994) determined that  $E(B-V)_{\text{star}} = 0.44E(B-V)_{\text{neb}}$ , based on the assumption that the nebular component follows a Galactic extinction curve (i.e.  $R_V = 3.1$ ) and that the stellar continuum component followed the Calzetti et al. (1994) attenuation law. Under this prescription the Calzetti et al. (1994) result indicates that  $A_{\text{star}} \approx 0.59 \times A_{\text{neb}}$  at  $\lambda_{\text{rest}} = 6563$  (Calzetti 2001).

Whether or not a significant difference between stellar continuum and nebular reddening persists in high-redshift star-forming galaxies is still a matter of debate (e.g. Wuyts et al. 2013; Kashino et al. 2013; Price et al. 2014). Here we adopt the results of Kashino et al. (2013), who investigated nebular versus stellar attenuation in a sample of 89 star-forming galaxies at  $1.4 < z < 1.7$ , using FMOS near-IR spectra. Assuming that both nebular and continuum attenuation followed the Calzetti et al. (2000) law, Kashino et al. (2013) found that  $E(B-V)_{\text{star}} = f \times E(B-V)_{\text{neb}}$ , with  $f$  in the range  $0.69 < f < 0.83$ . Based on these results we adopt a value of  $f = 0.76$ , noting that this is somewhat higher than the value of  $f = 0.54^{+0.13}_{-0.10}$  derived for  $z \approx 1.4$  star-forming galaxies by Price et al. (2014).

Consequently, in Fig. 5 the  $A_{1600}-M_*$  relations for Garn & Best (2010), Ibar et al. (2013) and Kashino et al. (2013) were derived by first multiplying their determinations of nebular attenuation by  $f = 0.76$  to obtain an estimate of the continuum attenuation at  $\lambda_{\text{rest}} = 6563$ , before assuming that  $A_{1600} = 3 \times A_{6563}$ , as appropriate for the Calzetti et al. (2000) attenuation law. As part of this calculation, the

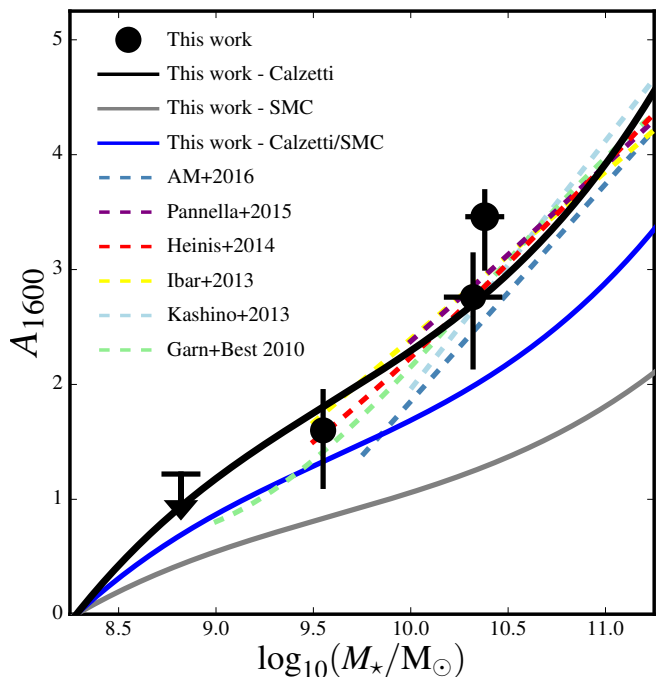


**Figure 5.** UV attenuation ( $A_{1600}$ ) versus stellar mass. The black data points show our estimates of  $A_{1600}$  within the same stellar-mass bins shown in Figs. 1 and 3. The value of  $A_{1600}$  in each mass bin has been calculated by converting between IRX and  $A_{1600}$  using equation (7). The solid black and grey lines show predicted  $A_{1600}-M_*$  relations, based on combining our fit to the  $\beta-M_*$  relation (see Fig. 4a) with a Calzetti-like (black) or SMC-like (grey) dust law. The solid blue line shows the predicted  $A_{1600}-M_*$  relation for a dust law with an intermediate UV slope to the Calzetti and SMC-like dust laws (blue dashed line in Fig. 3). The remaining dashed lines show  $A_{1600}-M_*$  relations derived from a number of different studies from the literature (see text for details). These  $A_{1600}-M_*$  relations have only been plotted over the mass range where they are properly constrained.

stellar-mass estimates provided by Ibar et al. (2013) and Kashino et al. (2013) were reduced by 0.22 dex to convert from a Salpeter (1955) to a Chabrier (2003) IMF and the stellar-mass estimates of Garn & Best (2010) were reduced by 0.03 dex to convert from a Kroupa (2001) IMF to a Chabrier (2003) IMF. The  $A_{1600}-M_*$  relations plotted in Fig. 5 for Garn & Best (2010) and Ibar et al. (2013) are based on our corrected versions of the functional forms they presented for the  $A_{H\alpha}-M_*$  relation. In contrast, the dashed curve shown in Fig. 5 for Kashino et al. (2013) is our linear fit to corrected versions of their binned  $A_{H\alpha}$  values as a function of stellar mass.

After making the corrections between nebular attenuation ( $A_{H\alpha}$ ) and stellar continuum attenuation in the UV ( $A_{1600}$ ), the results of Garn & Best (2010), Ibar et al. (2013) and Kashino et al. (2013) are in good agreement with the more direct determinations of Álvarez-Márquez et al. (2016), Pannella et al. (2015) and Heinis et al. (2014)<sup>3</sup>. Notably, despite the wide variety of different data sets, redshift ranges and methodologies represented, there is actually remarkably good agreement on the form of the  $A_{1600}-M_*$  relation, particularly at high stellar mass. The results of the different studies

<sup>3</sup> This would not be true based on the SMC extinction curve, which predicts  $A_{1600}$  values approximately two times higher ( $A_{1600} = 5.5 \times A_{6563}$ ).

shown in Fig. 5 indicate that galaxies with  $M_* \approx 10^{10} M_\odot$  experience  $A_{1600} \approx 2$  magnitudes of UV attenuation on average, which rises to  $A_{1600} \approx 4$  magnitudes of attenuation at  $M_* \approx 10^{11} M_\odot$ . It can clearly be seen from Fig. 5 that both our stacking results (black data points) and the predicted  $A_{1600}-M_*$  relation based on combining the  $\beta-M_*$  relation presented in Fig. 4a with the Calzetti et al. (2000) attenuation law (solid black curve) are fully consistent with this consensus.

Finally, it is also clear from Fig. 5 that the  $A_{1600}-M_*$  relations predicted by both an SMC-like dust law (grey solid line) and a dust law with a UV slope intermediate to the SMC and Calzetti dust laws (solid blue line) are inconsistent with our new results and those in the literature. Note that this conclusion regarding the SMC-like dust law is not significantly affected by our assumption that  $\beta_{\text{int}} = -2.3$ , since even shifting to  $\beta_{\text{int}} = -2.6$  only increases the vertical normalization of the SMC-like relation by  $\Delta A_{1600} \approx 0.3$  mag.

## 6 THE IRX- $M_*$ RELATION

In Fig. 6 we show the IRX- $M_*$  relation for star-forming galaxies at  $z \approx 2.5$ . In addition to our new results we also plot the results derived by a number of other studies, the details of which have been previously described in Sections 4 and 5.

Given the growing consensus in the literature that it is fundamentally stellar mass that drives UV attenuation, and therefore detectability at FIR, sub-mm and mm-wavelengths (e.g. Heinis et al. 2013; Pannella et al. 2015; Álvarez-Márquez et al. 2016; Dunlop et al. 2017; Bouwens et al. 2016; Reddy et al. 2018), it is arguable that the IRX- $M_*$  relation is physically more interesting than the IRX- $\beta$  relation. Excluding the most heavily obscured sources, the direct mapping between IRX and  $A_{1600}$  means that both relations provide a useful method for estimating a physical quantity ( $A_{1600}$ ), which is not directly observable.

Within this context, the IRX- $\beta$  relation has the advantage of being based on a straightforward observable ( $\beta$ ), in contrast to the IRX- $M_*$  relation, which is based on a derived quantity, namely the stellar mass. However, the much shallower form of the IRX- $M_*$  relation means that, in reality, it is the derived stellar mass that is likely to provide the cleanest prediction of UV attenuation.

An illustration of this is provided by considering a star-forming galaxy with  $\log(M_*/M_\odot) = 10.0$  and  $\beta = -1.15$  (see Fig. 4a). According to both the IRX- $\beta$  and IRX- $M_*$  relations based on Calzetti-like attenuation (black curves in Fig. 1 and Fig. 6) this galaxy should have  $\log(\text{IRX}) = 1.1$ . However, if we assume that representative uncertainties on the  $\beta$  and  $\log(M_*/M_\odot)$  measurements are  $\pm 0.3$  and  $\pm 0.3$  dex respectively, the IRX- $\beta$  relation implies that  $\log(\text{IRX}) = 1.1 \pm 0.3$ , whereas the IRX- $M_*$  relation implies that  $\log(\text{IRX}) = 1.1 \pm 0.15$ . As a consequence, the estimate of UV attenuation derived from the IRX- $M_*$  relation carries half the uncertainty of that derived from the IRX- $\beta$  relation (i.e.  $A_{1600} = 2.3 \pm 0.3$  mag compared to  $A_{1600} = 2.3 \pm 0.6$  mag).

It is clear from Fig. 6 that our predicted IRX- $M_*$  relation based on Calzetti-like dust attenuation (solid black curve) is in excellent agreement with the combined literature data set at  $\log(M_*/M_\odot) \geq 10$ . In the mass interval  $9.5 < \log(M_*/M_\odot) < 10$  the predicted IRX- $M_*$  relation is in good agreement with our stacked data point at  $\log(M_*/M_\odot) = 9.6$  and the data from Heinis et al. (2014), but in general appears to overpredict the combined literature data by  $\approx 0.2$  dex.

In contrast, it is clear that the IRX- $M_*$  relation predicted by

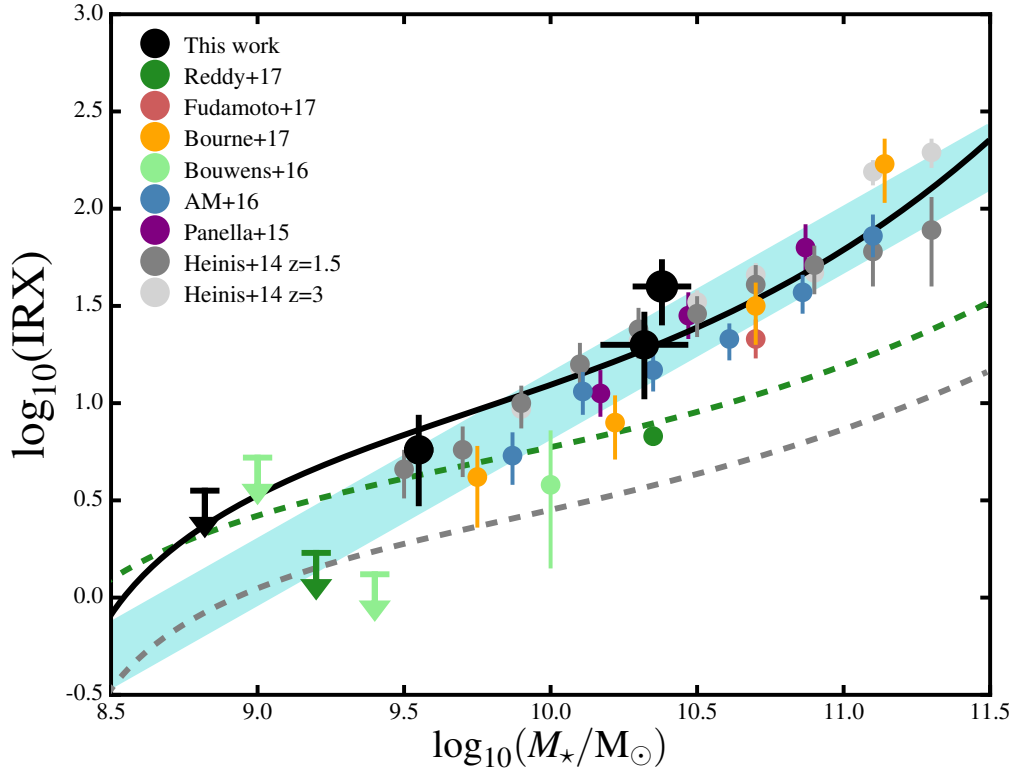


**Figure 6.** The IRX– $M_*$  relation for star-forming galaxies at  $z \approx 2.5$ . In addition to our new results, based on stacking the 1.3-mm ALMA data within the HUDF (black data points), we also plot results derived by Reddy et al. (2018), Fudamoto et al. (2017), Bourne et al. (2017), Bouwens et al. (2016), Álvarez-Márquez et al. (2016), Pannella et al. (2015) and Heinis et al. (2014). The solid black and dashed grey lines show predicted IRX– $M_*$  relations based on combining our fit to the  $\beta$ – $M_*$  relation (see Fig. 4a) with the IRX– $\beta$  relations based on either a Calzetti-like (black) or SMC-like (grey) dust law (assuming  $\beta_{\text{int}} = -2.3$ ). The dark green dashed line is the equivalent IRX– $M_*$  prediction based on the SMC-like IRX– $\beta$  relation derived by Reddy et al. (2018), which assumes  $\beta_{\text{int}} = -2.62$ . The shaded blue region represents our linear  $\log(\text{IRX}) - \log(M_*/M_\odot)$  fit to the combined data set and its associated  $1\sigma$  scatter.

an SMC-like extinction law with  $\beta_{\text{int}} = -2.3$  (grey dashed line) is a very poor match to the literature data, underpredicting the observed IRX values by  $\approx 0.4$  dex at  $\log(M_*/M_\odot) \approx 9.5$  and by  $\approx 1.0$  dex at  $\log(M_*/M_\odot) \approx 11.0$ . The situation is improved somewhat if, following Reddy et al. (2018), the SMC-like prediction is changed to assume that  $\beta_{\text{int}} = -2.62$  (green dashed line). In this case, the SMC-like IRX– $M_*$  relation does a good job of reproducing the literature data at  $\log(M_*/M_\odot) \approx 9.5$ . However, it can be seen that the SMC-like relation still does a very poor job of reproducing the literature data at  $\log(M_*/M_\odot) \geq 10$ , underpredicting the observed IRX values by  $\approx 0.6$  dex at  $\log(M_*/M_\odot) \approx 11$ .

The blue shaded area in Fig. 6 represents our best-fitting linear relationship between  $\log(M_*/M_\odot)$  and  $\log(\text{IRX})$  for those data-points at  $\log(M_*/M_\odot) \geq 9.5$ . This has the following form:

$$\log(\text{IRX}) = 0.85(\pm 0.05) \log\left(\frac{M_*}{10^{10} M_\odot}\right) + 0.99(\pm 0.03), \quad (18)$$

where the width of the shaded region illustrates the  $1\sigma$  scatter associated with the best-fitting relation ( $\approx 0.17$  dex). It can be seen from Fig. 6 that this linear relation provides an excellent description of the combined data set, such that a more complicated functional form is not justified. We note that our best-fitting relation is very similar to that previously derived by Álvarez-Márquez et al. (2016) at  $z \approx 3$  and somewhat steeper than, but still consistent with, the

relation derived by Heinis et al. (2014) at  $z \approx 1.5$ . Finally, we note that our best-fitting relation also provides a good description of the IRX– $M_*$  data for  $1.5 < z < 2.5$  star-forming galaxies derived from the 3D-HST photometric catalogues by Whitaker et al. (2014), using  $L_{\text{IR}}$  values based on *Spitzer* 24- $\mu\text{m}$  data.

In general, it can be seen from Fig. 6 that the IRX– $M_*$  relations based on SMC-like extinction curves (grey and green dashed lines) have fundamentally the wrong shape to provide a good description of the literature data over a wide range in stellar mass. This is equivalent to saying that the slope of the effective attenuation curve needs to be closer to  $dA_{1600}/d\beta \approx 2$  than  $dA_{1600}/d\beta \approx 1$  in order to reproduce the observed IRX– $M_*$  data. Therefore, it appears that the effective dust attenuation experienced by star-forming galaxies at  $z \approx 2.5$  is much more similar to the Calzetti et al. (2000) attenuation law than an SMC-like extinction curve, at least at  $\log(M_*/M_\odot) \geq 9.75$ .

Given the sensitivity limits of currently available data, it is clear from Figs. 5 and 6 that the form of the dust attenuation law at  $\log(M_*/M_\odot) \leq 9.75$  is still very poorly constrained. However, given the constraints that do exist, it appears likely that the IRX– $M_*$  relation will fall below the Calzetti-like prediction at  $\log(M_*/M_\odot) \approx 9.0$ . If confirmed, this would indicate that there is a shift towards a steeper attenuation law with decreasing stellar mass, something which could plausibly be connected to a mass-dependent change in the gas/dust geometry (e.g. Paardekooper et al.



2015). ALMA imaging at sub-mm wavelengths with an effective dust continuum sensitivity a factor 3–5 deeper than the 1.3-mm mosaic exploited here could potentially address this question.

### 6.1 Star-formation rate density

Armed with our best-fitting IRX– $M_*$  relation (equation 18) it is possible to estimate the total (UV+IR) star-formation rate density at  $z \approx 2.5$  using our sample of  $2 < z < 3$  star-forming galaxies in the HUDF. For each galaxy within the HUDF sample with stellar-mass  $\log(M_*/M_\odot) \geq 8.5$ , we calculate the SFR<sub>TOT</sub> (UV+IR) assuming that

$$\text{SFR}_{\text{UV+IR}} = \text{SFR}_{\text{UV}}(1 + \text{IRX}), \quad (19)$$

where SFR<sub>UV</sub> and IRX are calculated from equation (10) and equation (18) respectively, and  $L_{\text{UV}}$  and  $M_*$  are derived from the best-fitting SED template to its UV-to-midIR photometry. By simply summing the contribution of each galaxy, and taking the co-moving volume of the HUDF to be  $1.5 \times 10^4 \text{ Mpc}^3$ , we arrive at an estimate of  $\log(\rho_{\text{UV+IR}}/M_\odot\text{yr}^{-1}\text{Mpc}^{-3}) = -1.04 \pm 0.09$ , where the uncertainty has been calculated using bootstrap re-sampling. This estimate is in excellent agreement with the value calculated by Dunlop et al. (2017) and the  $\rho_{\text{SFR}}(z)$  fitting formula derived by Behroozi et al. (2013). Our estimate is somewhat higher than the  $\rho_{\text{SFR}}(z)$  fitting formula derived by Madau & Dickinson (2014), but is actually very consistent with their compilation of data at  $z \approx 2.5$ . If we also account for the fact that, in the HUDF at least, the best-fitting IRX– $M_*$  relation underpredicts the SFR<sub>IR</sub> values of the most heavily obscured sources by a factor of  $\approx 2$ , our SFRD estimate increases to  $\log(\rho_{\text{UV+IR}}/M_\odot\text{yr}^{-1}\text{Mpc}^{-3}) = -0.94 \pm 0.13$ .

## 7 DISCUSSION

The results presented in the last two sections strongly suggest that the effective attenuation law experienced by star-forming galaxies at  $z \approx 2.5$  lies closer to the Calzetti et al. (2000) attenuation law than the SMC-like extinction law.

As discussed in Section 1, it is expected that the attenuation law applicable to integrated galaxy photometry should be substantially greyer than a SMC-like extinction law if the local extinction law is SMC-like. Although it is impossible to directly measure the extinction law in  $2 < z < 3$  star-forming galaxies, supporting evidence for this scenario is provided by the direct extinction curve measurements from gamma-ray burst (GRB) afterglows. These studies typically show that GRB extinction curves are similar to the SMC extinction curve (e.g. Zafar et al. 2011), at least at low-to-moderate levels of extinction (i.e.  $A_V \leq 0.65$ ), exactly as required to produce a Calzetti-like attenuation curve.

However, despite the consistency with the results presented here, it is clear from Fig. 3 that the majority of studies in the literature find that the IRX– $\beta$  relation displayed by star-forming galaxies at this epoch falls significantly below what would be expected for the Calzetti et al. (2000) attenuation law. This presents a significant problem, given that it is clearly necessary to have consistency between the IRX– $\beta$  and IRX– $M_*$  relations.

In Section 4 we proposed three potential solutions to the apparent disagreement between the IRX– $\beta$  relations determined by various literature studies and the IRX– $\beta$  relation expected if the underlying attenuation law was Calzetti-like. The first, and most straightforward, solution is to accept that the effective attenuation

law has an intermediate dust slope of  $dA_{1600}/d\beta \approx 1.45$ . However, although this is able to do a reasonable job of reproducing the observed IRX– $\beta$  data, it is unable to reproduce the observed  $A_{1600} - M_*$  or IRX– $M_*$  relations (see Fig. 5).

The second option is to adopt an SMC-like dust law in combination with an ultra-blue value of intrinsic UV slope (i.e.  $\beta_{\text{int}} = -2.62$ ), as proposed by Reddy et al. (2018). However, as shown in Fig. 6, the IRX– $M_*$  relation predicted by an SMC-like dust law, regardless of the assumed value of  $\beta_{\text{int}}$ , does not have the correct shape to reproduce the observed data over a large dynamic range in stellar mass.

The third and final option proposed in Section 4 is that the underlying dust law at  $z \approx 2.5$  is indeed close to the Calzetti et al. (2000) attenuation law, and that the IRX– $\beta$  relations derived by previous studies are biased towards low values of IRX at red values of  $\beta$ . In this scenario, the bias in the IRX– $\beta$  results is directly caused by uncertainties in measuring individual values of  $\beta$ , in combination with using mean IRX values binned by  $\beta$ . In this section we investigate this remaining option in more detail.

### 7.1 Bias due to UV slope uncertainty

The IRX– $\beta$  plot is vulnerable to bias when plotting results binned by  $\beta$  due to a combination of three elements: the relatively large uncertainties associated with observational determinations of  $\beta$ , the steepness of the stellar-mass function and the steepness of the IRX– $\beta$  relationship itself.

The steepness of the stellar-mass function means that any given sample of star-forming galaxies must be dominated by galaxies close to the stellar-mass limit of the sample. Moreover, due to the strong correlation between stellar mass and dust attenuation, these low-mass galaxies will also have the bluest values of  $\beta$  and the smallest values of IRX. Furthermore, due to the large uncertainties inherent in measuring  $\beta$  photometrically, even relatively modest amounts of photometric scatter will result in a small fraction of these objects being measured as having much redder values of  $\beta$ . Unfortunately, due to the dominance of intrinsically blue objects ensured by the stellar-mass function, even a small fraction of misclassified blue galaxies can lead to significant problems when choosing to bin-up the IRX– $\beta$  plane in terms of the *observed* values of  $\beta$ .

As a specific example, when considering the typical value of IRX for galaxies with observed values of  $\beta$  in the range  $-1.5 < \beta < -1.0$ , this  $\beta$  bin will inevitably contain significant numbers of galaxies whose actual value of observed  $\beta$  (i.e. with perfect photometry) should be  $\beta \approx -2$ . Given the steepness of the IRX– $\beta$  relationship, these contaminants will carry significantly smaller values of IRX (factor of  $\approx 4$  for Calzetti-like dust attenuation) than suggested by their measured UV-slope of  $\beta \approx -1.25$ . Fundamentally, it is this contamination from objects scattered towards redder values of  $\beta$  which inevitably results in the apparent suppression of the average IRX values when binning samples by observed  $\beta$ . Crucially, as explained in the previous section, the shallower slope of the IRX– $M_*$  relation means that this bias should not apply to determinations of the IRX– $\beta$  relation using samples binned by stellar mass.

### 7.2 IRX simulation

To investigate this problem further, we have run a simple simulation to investigate whether IRX– $\beta$  results in the recent literature can be reproduced by modelling the bias discussed above. We have focused

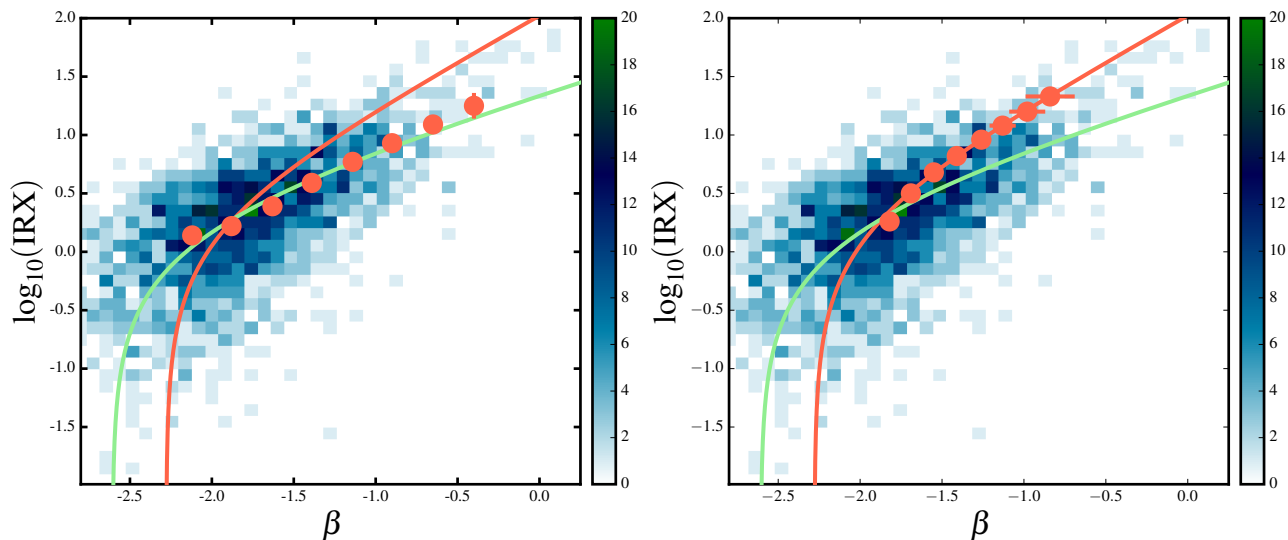


**Figure 7.** Simulations of the IRX– $\beta$  relation. Both panels show a 2D histogram of a single realisation of our IRX– $\beta$  simulation, along with the input IRX– $\beta$  relation (red line) and the IRX– $\beta$  relation recently determined for  $1.5 < z < 2.5$  star-forming galaxies (green line) by Reddy et al. (2018). Each realisation of the simulation features 3545 simulated galaxies to match the size of the observed sample of Reddy et al. (2018). In the left-hand panel, the red data points show the mean binned values of IRX determined from 1000 realisations, when binning the simulation output in terms of  $\beta$ . The eight data points correspond to  $\Delta\beta = 0.25$  bins spanning the range  $-2.25 \leq \beta \leq -0.25$ . In the right-hand panel the red data points show the equivalent results when the output is binned in terms of stellar mass. The eight data points shown in the right-hand panel correspond (left-to-right) to the stellar-mass range  $8.75 \leq \log(M_*/M_\odot) \leq 10.75$ , in bins of width 0.25 dex. It can be seen that the IRX– $\beta$  relationship recovered when binning in terms of  $\beta$  is biased, a problem that does not occur when binning in terms of stellar mass.

this simulation on reproducing the results of Reddy et al. (2018), but the same arguments apply to any of the studies discussed in Section 4. The aim of this experiment is simply to ascertain whether or not an IRX– $\beta$  relation that is apparently consistent with an SMC-like dust law and ultra-blue intrinsic UV slope, can in fact be generated from a galaxy sample that is reddened by the Calzetti et al. (2000) attenuation law.

The first step in this process is to define a fiducial intrinsic SED template for each of the synthetic galaxies. Following Reddy et al. (2018), we fit the SEDs of the objects within our HUDF galaxy sample with constant star-formation rate (CSFR) stellar population models based on a BPASSv2-100bin-0.002 simple stellar population (Kroupa 2001 IMF with a  $100 M_\odot$  cut-off,  $Z = 0.002^4$  and binary stars included), with accompanying nebular continuum and line emission predictions from CLOUDY (Ferland et al. 2013). Full details about the production of these models can be found in Cullen et al. (2017). Based on the fits to our HUDF sample, the typical low-mass star-forming galaxy at  $z \approx 2.5$  is best-fit by a CSFR model with an age of 400 Myr (mass-weighted age of 200 Myr) and an intrinsic UV slope of  $\beta_{\text{int}} = -2.28$ . This is therefore the fiducial intrinsic SED assumed for every synthetic galaxy. We note that the typical best-fitting template based on the same models without the nebular continuum has an intrinsic UV slope of  $\beta_{\text{int}} = -2.48$ .

After deciding on a fiducial SED, the next step is to draw a synthetic population of  $z = 2.5$  galaxies from the stellar-mass function of star-forming galaxies at this redshift, which is assumed to follow a Schechter function with the following parameters:  $\log(\phi^*/\text{Mpc}^{-3}) = -3.9$ ,  $\log(M_*/M_\odot) = 11.0$ ,  $\alpha = -1.7$ . These parameters are consistent with the results of both Tomczak et al. (2014) and Davidzon et al. (2017). Each synthetic galaxy was then

allocated a value of dust attenuation ( $A_{1600}$ ), based on our prediction for the  $A_{1600}$ – $M_*$  relation (black curve in Fig. 5), with an assumed Gaussian scatter of  $\sigma = 0.3$  mag (Garn & Best 2010). The value of IRX for each synthetic galaxy could then be calculated via equation (7).

According to the properties of the fiducial SED, and our modelling of the full  $2 < z < 3$  star-forming galaxy sample, the value of intrinsic UV-slope ( $\beta_{\text{int}}$ ) associated with each synthetic galaxy was randomly drawn from a Gaussian distribution centred on  $\beta_{\text{int}} = -2.28$  with  $\sigma = 0.15$ . The exact value of the observed UV-slope was then calculated by applying the Calzetti et al. (2000) attenuation law with the appropriate  $A_{1600}$  value. The actual observed value of the UV-slope (i.e. the measured value) was then calculated by applying a measurement uncertainty ( $\sigma_\beta$ ) designed to reflect the impact of photometric scatter. The value of  $\sigma_\beta$  is a free parameter which was varied in order to determine the level of  $\beta$  uncertainty required to reproduce the Reddy et al. (2018) results.

### 7.2.1 Simulation output

The output of a single realisation of our simulation is shown in Fig. 7, where we have applied the  $H < 27$  and  $m_{1700 \times (1+z)} < 27$  cuts adopted by Reddy et al. (2018) and applied a constant value of  $\sigma_\beta = 0.35$ . Both panels show the same 2D histogram of the simulation output on the IRX– $\beta$  plane, with the red and green curves showing the input IRX– $\beta$  relation and the observed relation from Reddy et al. (2018) respectively. In the left-hand panel, the red data points show the mean binned values of IRX produced by 1000 realisations, binning in  $\beta$ . The eight data points correspond to  $\Delta\beta = 0.25$  bins spanning the range  $-2.25 \leq \beta \leq -0.25$ . In the right-hand panel the red data points show the equivalent information based on binning in stellar mass. The eight data points in this plot

<sup>4</sup> This is  $0.1Z_\odot$  for  $Z_\odot = 0.02$  or  $0.14Z_\odot$  for  $Z_\odot = 0.014$  (Asplund et al. 2009).

correspond to bins of width 0.25 dex, spanning (left-to-right) the stellar-mass range  $8.75 \leq \log(M_*/M_\odot) \leq 10.75$ .

The results shown in the left-hand panel of Fig. 7 provide a clear illustration of the impact of scatter on the measured values of UV-slope. Despite the fact that the input simulated galaxies follow the IRX- $\beta$  relation expected for the Calzetti et al. (2000) attenuation law (red curve), when the sample is binned by observed  $\beta$ , the binned values of IRX are significantly suppressed. Notably, for a value of  $\sigma_\beta = 0.35$ , the output IRX- $\beta$  relation appears to follow the SMC-like IRX- $\beta$  relation with  $\beta_{\text{int}} = -2.62$  (green curve) determined by Reddy et al. (2018).

In contrast, the results shown in the right-hand panel of Fig. 7 show the inherent advantages of binning by stellar mass. In this case, it can be seen that the recovered IRX- $\beta$  relation closely follows the input IRX- $\beta$  relation. In the simulation we have assumed a scatter of 0.3 dex in stellar mass, but the input IRX- $\beta$  relation is still recovered with reasonable accuracy for an assumed scatter as high as 0.5 dex.

### 7.3 UV-slope uncertainty

The results of our simplified simulation indicate that a typical uncertainty of  $\sigma_\beta \approx 0.3\text{--}0.4$  is sufficient to bias an input IRX- $\beta$  relation consistent with Calzetti-like attenuation, into an observed IRX- $\beta$  relation which closely mimics that expected for an SMC-like extinction law, combined with an ultra-blue value of intrinsic UV slope. Consequently, it is of obvious interest to determine whether or not this level of  $\beta$  uncertainty is plausible.

In this study, and in Reddy et al. (2018), the UV spectral slope is measured by fitting power laws to the available rest-frame UV photometry. However, due to the need to exclude filters contaminated by Ly $\alpha$  emission and the requirement to restrict the long-wavelength anchor to  $\lambda_{\text{rest}} < 2580\text{\AA}$  (Calzetti et al. 1994), it is often the case that there are only two or three filters that sample the correct wavelength interval. This problem is particularly acute when dealing with the wide filters typically adopted for *HST* ACS imaging. For example, for the purposes of our simulated sample at  $z \approx 2.5$ , we have calculated synthetic photometry in the same *HST* filters available in the HUDF and GOODS fields. In this case, the only two filters available with which to obtain a clean measurement of  $\beta$  are F606W ( $V_{606}$ ) and F775W ( $i_{775}$ ). In this situation it is straightforward to analytically determine the relationship between the best-fitting power law and the  $V_{606} - i_{775}$  colour:

$$\beta = 3.52(V_{606} - i_{775}) - 2.0, \quad (20)$$

where the multiplicative constant is determined by the pivot wavelengths of the two filters. It can then be seen that the typical uncertainty on  $\beta$  is given by

$$\sigma_\beta = 3.52\sqrt{\sigma_{606}^2 + \sigma_{775}^2}, \quad (21)$$

where  $\sigma_{606}$  and  $\sigma_{775}$  are the uncertainties on the  $V_{606}$  and  $i_{775}$  magnitudes. If we further assume that the F606W and F775W imaging is of equal depth, equation (20) implies that the value of  $\sigma_\beta = 0.35$  employed in our simulation is equivalent to assuming  $\approx 15\sigma$  detections in both filters. It would therefore appear reasonable to assume that most studies of the IRX- $\beta$  relation at this epoch are subject to uncertainties of this level, or greater.

### 7.4 Summary

Although the simulation results we have presented here are somewhat simplified, they are sufficient to illustrate the general point that

a relatively small amount of uncertainty in measuring  $\beta$  is sufficient to produce biased results in the IRX- $\beta$  plane, when binning by  $\beta$ . Although clearly not definitive, this does offer a plausible explanation for why many IRX- $\beta$  results in the literature do not follow the expected relation for Calzetti-like dust attenuation whereas, in general, the IRX- $M_*$  results do.

## 8 CONCLUSIONS

In this paper we have presented the results of a study of the IRX- $\beta$  and IRX- $M_*$  relations for star-forming galaxies at  $2 < z < 3$ , based on the deep 1.3-mm ALMA mosaic of the HUDF presented by Dunlop et al. (2017). In addition to the new ALMA-based results, we have determined the empirical relationship between UV slope and stellar mass for a large, mass-complete, sample of  $2 < z < 3$  star-forming galaxies selected over an area of  $\approx 1 \text{ deg}^2$ . Armed with this information, and a compilation of literature results, we have investigated the relationship between stellar mass and UV attenuation in star-forming galaxies at this crucial epoch. Our main conclusions can be summarised as follows:

(i) A stacking analysis within the 1.3-mm ALMA mosaic of the HUDF indicates that star-forming galaxies at  $2 < z < 3$  follow an IRX- $\beta$  relation fully consistent with a relatively grey, Calzetti-like, dust attenuation law. In contrast, our new results are inconsistent with a dust law as steep in the UV as the SMC extinction law.

(ii) Based on a large, mass complete, sample of star-forming galaxies at  $2 < z < 3$ , we find that UV slope is a smoothly increasing function of stellar mass. Our determination of the  $\beta - M_*$  relation is well described by a third-order polynomial:  $\beta = -1.136 + 0.589X + 0.130X^2 + 0.106X^3$ ; where  $X = \log(M_*/10^{10} M_\odot)$ . Furthermore, our SED modelling of the star-forming galaxy sample indicates that the intrinsic UV slope is fully consistent with a value of  $\beta_{\text{int}} \approx -2.3$  over the full  $8.50 < \log(M_*/M_\odot) < 11.5$  stellar-mass range.

(iii) Armed with the new empirical determination of the  $\beta - M_*$  relation, it is possible to derive the expected relationship between  $A_{1600}$  and stellar mass for any assumed dust law. By combining our new ALMA-based results with previous literature studies, we demonstrate that the  $A_{1600} - M_*$  relation at  $z \approx 2.5$  is consistent with Calzetti-like attenuation at  $\log(M_*/M_\odot) \geq 9.75$ .

(iv) By combining the observed  $\beta - M_*$  relation with an assumed dust law, it is also possible to predict the form of the IRX- $M_*$  relation. We show that our new ALMA-based results, and the majority of recent literature results, are also consistent with the IRX- $M_*$  relation expected for Calzetti-like dust attenuation at  $\log(M_*/M_\odot) \geq 9.75$ .

(v) We find that the currently available IRX- $M_*$  data at  $z \approx 2.5$  can be well described by a relationship of the form:  $\log(\text{IRX}) = 0.85(\pm 0.05) \log\left(\frac{M_*}{10^{10} M_\odot}\right) + 0.99(\pm 0.03)$ , with an associated  $1\sigma$  scatter of  $\pm 0.17$  dex.

(vi) Our results indicate that an IRX- $M_*$  relation based on an SMC-like dust law, irrespective of the assumed value of the intrinsic UV slope ( $\beta_{\text{int}}$ ), has the wrong shape to adequately reproduce the observed IRX data over a large dynamic range in stellar mass. At stellar masses of  $\log(M_*/M_\odot) \leq 9.75$  the situation is much more uncertain, and deeper continuum imaging with ALMA will be required to determine the relationship between UV attenuation and stellar mass.

(vii) We employ a simple simulation to demonstrate that the uncertainty in individual  $\beta$  measurements, combined with binning-up samples by  $\beta$ , is sufficient to significantly bias measurements of the IRX- $\beta$  relation. Crucially, our simulation also demonstrates that

this bias does not significantly affect determinations of the IRX– $\beta$  relation based on binning samples by stellar mass.

(viii) The results of our simulation provide a plausible mechanism to explain the apparently contradictory IRX– $\beta$  and IRX– $M_*$  results in the literature, and demonstrate that both sets of observational results are fully consistent with a relatively grey, Calzetti-like, dust attenuation law.

(ix) The combination of observational and simulated results strongly indicate that, based on typical measurement uncertainties, it is stellar mass, rather than UV spectral slope, that provides the most accurate, least biased, proxy for the absolute level of UV attenuation experienced by star-forming galaxies.

## ACKNOWLEDGEMENTS

RJM, JSD, FC, NB, PNB and SK acknowledge the support of the UK Science and Technology Facilities Council. RAAB acknowledges the support of the Oxford Centre for Astrophysical Surveys which is funded through generous support from the Hintze Family Charitable Foundation. JEG thanks the Royal Society for support. MJM acknowledges the support of the National Science Centre, Poland through the POLONEZ grant 2015/19/P/ST9/04010 and the UK Science and Technology Facilities Council. This project has received funding from the European Union’s Horizon 2020 research and innovation programme under the Marie Skłodowska-Curie grant agreement No. 665778. WR is supported by JSPS KAKENHI Grant Number JP15K17604 and the Thailand Research Fund/Office of the Higher Education Commission Grant Number MRG6080294. ALMA is a partnership of ESO (representing its member states), NSF (USA) and NINS (Japan), together with NRC (Canada), and ASIAA (Taiwan), and KASI (Republic of Korea), in cooperation with the Republic of Chile. The Joint ALMA Observatory is operated by ESO, AUI/NRAO and NAOJ. This work is based in part on observations made with the NASA/ESA *Hubble Space Telescope*, which is operated by the Association of Universities for Research in Astronomy, Inc; under NASA contract NAS5-26555. This work is also based in part on observations made with the *Spitzer Space Telescope*, which is operated by the Jet Propulsion Laboratory, California Institute of Technology under NASA contract 1407. *Herschel* is an ESA space observatory with science instruments provided by European-led Principal Investigator consortia and with important participation from NASA.

## References

- Álvarez-Márquez J., et al., 2016, *A&A*, **587**, A122  
 Ashby M. L. N., et al., 2013, *ApJ*, **769**, 80  
 Asplund M., Grevesse N., Sauval A. J., Scott P., 2009, *ARA&A*, **47**, 481  
 Beckwith S. V. W., et al., 2006, *AJ*, **132**, 1729  
 Behroozi P. S., Wechsler R. H., Conroy C., 2013, *ApJ*, **770**, 57  
 Bourne N., et al., 2017, *MNRAS*,  
 Bouwens R. J., et al., 2011, *ApJ*, **737**, 90  
 Bouwens R. J., et al., 2012, *ApJ*, **754**, 83  
 Bouwens R. J., et al., 2014, *ApJ*, **793**, 115  
 Bouwens R. J., et al., 2016, *ApJ*, **833**, 72  
 Brammer G. B., et al., 2012, *ApJS*, **200**, 13  
 Bruzual G., Charlot S., 2003, *MNRAS*, **344**, 1000  
 Calzetti D., 2001, *PASP*, **113**, 1449  
 Calzetti D., Kinney A. L., Storchi-Bergmann T., 1994, *ApJ*, **429**, 582  
 Calzetti D., Armus L., Bohlin R. C., Kinney A. L., Koornneef J., Storchi-Bergmann T., 2000, *ApJ*, **533**, 682  
 Capak P. L., et al., 2015, *Nature*, **522**, 455  
 Chabrier G., 2003, *PASP*, **115**, 763  
 Coppin K. E. K., et al., 2015, *MNRAS*, **446**, 1293  
 Cullen F., Cirasuolo M., Kewley L. J., McLure R. J., Dunlop J. S., Bowler R. A. A., 2016, *MNRAS*, **460**, 3002  
 Cullen F., McLure R. J., Khochfar S., Dunlop J. S., Dalla Vecchia C., 2017, *MNRAS*, **470**, 3006  
 Dahlen T., et al., 2013, *ApJ*, **775**, 93  
 Davidzon I., et al., 2017, *A&A*, **605**, A70  
 Dunlop J. S., et al., 2013, *MNRAS*, **432**, 3520  
 Dunlop J. S., et al., 2017, *MNRAS*, **466**, 861  
 Eldridge J. J., Stanway E. R., 2016, *MNRAS*, **462**, 3302  
 Ellis R. S., et al., 2013, *ApJ*, **763**, L7  
 Ferland G. J., et al., 2013, *Rev. Mex. Astron. Astrofis.*, **49**, 137  
 Finkelstein S. L., 2016, *Publ. Astron. Soc. Australia*, **33**, e037  
 Finkelstein S. L., et al., 2012, *ApJ*, **756**, 164  
 Fontana A., et al., 2014, *A&A*, **570**, A11  
 Fudamoto Y., et al., 2017, *MNRAS*, **472**, 483  
 Furusawa H., et al., 2016, *ApJ*, **822**, 46  
 Galametz A., et al., 2013, *ApJS*, **206**, 10  
 Garn T., Best P. N., 2010, *MNRAS*, **409**, 421  
 Geach J. E., et al., 2017, *MNRAS*, **465**, 1789  
 Gordon K. D., Clayton G. C., Misselt K. A., Landolt A. U., Wolff M. J., 2003, *ApJ*, **594**, 279  
 Guo Y., et al., 2013, *ApJS*, **207**, 24  
 Heinis S., et al., 2013, *MNRAS*, **429**, 1113  
 Heinis S., et al., 2014, *MNRAS*, **437**, 1268  
 Helou G., Khan I. R., Malek L., Boehmer L., 1988, *ApJS*, **68**, 151  
 Hudelot P., et al., 2012, *VizieR Online Data Catalog*, **2317**  
 Ibar E., et al., 2013, *MNRAS*, **434**, 3218  
 Illingworth G. D., et al., 2013, *ApJS*, **209**, 6  
 Kashino D., et al., 2013, *ApJ*, **777**, L8  
 Kennicutt R. C., Evans N. J., 2012, *ARA&A*, **50**, 531  
 Koekemoer A. M., et al., 2013, *ApJS*, **209**, 3  
 Kong X., Charlot S., Brinchmann J., Fall S. M., 2004, *MNRAS*, **349**, 769  
 Koprowski M. P., et al., 2016, *ApJ*, **828**, L21  
 Kroupa P., 2001, *MNRAS*, **322**, 231  
 Labbé I., et al., 2015, *ApJS*, **221**, 23  
 Laidler V. G., et al., 2007, *PASP*, **119**, 1325  
 Laporte N., et al., 2017, *ApJ*, **837**, L21  
 Lee K.-S., Alberts S., Atlee D., Dey A., Pope A., Jannuzi B. T., Reddy N., Brown M. J. I., 2012, *ApJ*, **758**, L31  
 Madau P., 1995, *ApJ*, **441**, 18  
 Madau P., Dickinson M., 2014, *ARA&A*, **52**, 415  
 McLeod D. J., McLure R. J., Dunlop J. S., Robertson B. E., Ellis R. S., Targett T. A., 2015, *MNRAS*, **450**, 3032  
 McLeod D. J., McLure R. J., Dunlop J. S., 2016, *MNRAS*, **459**, 3812  
 McLure R. J., et al., 2011, *MNRAS*, **418**, 2074  
 McLure R. J., et al., 2013, *MNRAS*, **432**, 2696  
 Meurer G. R., Heckman T. M., Calzetti D., 1999, *ApJ*, **521**, 64  
 Momcheva I. G., et al., 2016, *ApJS*, **225**, 27  
 Mortlock A., McLure R. J., Bowler R. A. A., McLeod D. J., Marmol-Queraltó E., Parsa S., Dunlop J. S., Bruce V. A., 2017, *MNRAS*, **465**, 672  
 Narayanan D., Davé R., Johnson B. D., Thompson R., Conroy C., Geach J., 2018, *MNRAS*, **474**, 1718  
 Nonino M., et al., 2009, *ApJS*, **183**, 244  
 Novak M., et al., 2017, *A&A*, **602**, A5  
 Oke J. B., Gunn J. E., 1983, *ApJ*, **266**, 713  
 Overzier R. A., et al., 2011, *ApJ*, **726**, L7  
 Paardekooper J.-P., Khochfar S., Dalla Vecchia C., 2015, *MNRAS*, **451**, 2544  
 Pannella M., et al., 2015, *ApJ*, **807**, 141  
 Pettini M., Kellogg M., Steidel C. C., Dickinson M., Adelberger K. L., Giavalisco M., 1998, *ApJ*, **508**, 539  
 Pope A., et al., 2017, *ApJ*, **838**, 137  
 Popping M., Puglisi A., Norman C. A., 2017, *MNRAS*, **472**, 2315  
 Prevot M. L., Lequeux J., Prevot L., Maurice E., Rocca-Volmerange B., 1984, *A&A*, **132**, 389



- Price S. H., et al., 2014, *ApJ*, 788, 86
- Reddy N. A., Erb D. K., Pettini M., Steidel C. C., Shapley A. E., 2010, *ApJ*, 712, 1070
- Reddy N. A., et al., 2015, *ApJ*, 806, 259
- Reddy N. A., et al., 2018, *ApJ*, 853, 56
- Rogers A. B., McLure R. J., Dunlop J. S., 2013, *MNRAS*, 429, 2456
- Rogers A. B., et al., 2014, *MNRAS*, 440, 3714
- Rujopakarn W., et al., 2016, *ApJ*, 833, 12
- Salmon B., et al., 2016, *ApJ*, 827, 20
- Salpeter E. E., 1955, *ApJ*, 121, 161
- Santini P., et al., 2015, *ApJ*, 801, 97
- Scoville N., Faisst A., Capak P., Kakazu Y., Li G., Steinhardt C., 2015, *ApJ*, 800, 108
- Seon K.-I., Draine B. T., 2016, *ApJ*, 833, 201
- Shapley A. E., et al., 2015, *ApJ*, 801, 88
- Speagle J. S., Steinhardt C. L., Capak P. L., Silverman J. D., 2014, *ApJS*, 214, 15
- Stanway E. R., Eldridge J. J., Becker G. D., 2016, *MNRAS*, 456, 485
- Stark D. P., 2016, *ARA&A*, 54, 761
- Steidel C. C., Strom A. L., Pettini M., Rudie G. C., Reddy N. A., Trainor R. F., 2016, *ApJ*, 826, 159
- Steinhardt C. L., et al., 2014, *ApJ*, 791, L25
- Strom A. L., Steidel C. C., Rudie G. C., Trainor R. F., Pettini M., Reddy N. A., 2017, *ApJ*, 836, 164
- Takeuchi T. T., Yuan F.-T., Ikeyama A., Murata K. L., Inoue A. K., 2012, *ApJ*, 755, 144
- Tomczak A. R., et al., 2014, *ApJ*, 783, 85
- Watson D., Christensen L., Knudsen K. K., Richard J., Gallazzi A., Michałowski M. J., 2015, *Nature*, 519, 327
- Whitaker K. E., et al., 2011, *ApJ*, 735, 86
- Whitaker K. E., et al., 2014, *ApJ*, 795, 104
- Williams R. J., Quadri R. F., Franx M., van Dokkum P., Labbé I., 2009, *ApJ*, 691, 1879
- Witt A. N., Gordon K. D., 2000, *ApJ*, 528, 799
- Wuyts S., et al., 2013, *ApJ*, 779, 135
- Zafar T., Watson D., Fynbo J. P. U., Malesani D., Jakobsson P., de Ugarte Postigo A., 2011, *A&A*, 532, A143

This paper has been typeset from a  $\text{\TeX}/\text{\LaTeX}$  file prepared by the author.